UNIVERSIDAD DE CHILE
FACULTAD DE CIENCIAS FÍSICAS Y MATEMÁTICAS
DEPARTAMENTO DE INGENIERÍA MATEMÁTICA

OPTIMIZATION OF THE ANISOTROPIC ELASTIC PROPERTIES OF A MECHANICAL METAMATERIAL FOR THE DESIGN OF WOODEN MUSICAL INSTRUMENTS.

TESIS PARA OPTAR AL GRADO DE MAGÍSTER EN CIENCIAS DE LA INGENIERÍA, MENCIÓN MATEMÁTICAS APLICADAS

MEMORIA PARA OPTAR AL TÍTULO DE INGENIERO CIVIL MATEMÁTICO

EMIR NICOLÁS CHACRA GARRIDO

PROFESOR GUÍA:
AXEL OSSES ALVARADO

PROFESOR CO-GUÍA:
JEAN-GABRIEL MINONZIO

MIEMBROS DE LA COMISIÓN:
JOCELYN DUNSTAN ESCUDERO
CAROLINA ESPINOZA OÑATE
SEBASTIÁN GONZÁLEZ BRIONES

SANTIAGO DE CHILE
2022

OPTIMIZACIÓN DE LAS PROPIEDADES ELÁSTICAS ANISOTRÓPICAS DE UN METAMATERIAL MECÁNICO PARA EL DISEÑO DE INSTRUMENTOS MUSICALES DE MADERA.

Los fabricantes de guitarras han lidiado siempre con la variabilidad de las propiedades de la madera, ya que dos placas cortadas del mismo tronco podrían tener un comportamiento acústico muy diferente. Además, el calentamiento global está reduciendo el hábitat de las maderas tradicionales para instrumentos (por ejemplo, el Abeto Engelmann), lo que provoca su escasez y un mayor coste de fabricación. Ambos hechos han inspirado la investigación de materiales alternativos. En esta tesis, se propone los metamateriales mecánicos de madera como un nuevo material para la fabricación de instrumentos, cuya geometría consiste en patrones de agujeros. Se estudia el efecto de las variaciones del patrón en las principales propiedades elásticas del metamaterial en las direcciones longitudinal y radial, a saber, E_L y E_R. Se descubre que el tamaño y la simetría de los agujeros, así como la distribución del tamaño de los agujeros, influyen directamente en estos parámetros y es posible sintonizarlos de forma independiente o ambos al mismo tiempo. Por último, se desarrolla un algoritmo de optimización para encontrar el mejor patrón para parámetros objetivo fijos, y se aplica con éxito el algoritmo en casos que se asemejan a las dos dificultades que inspiraron esta investigación. Se demuestra que los metamateriales mecánicos de madera pueden mejorar la respuesta de las maderas que naturalmente no son adecuadas para los instrumentos, tallando la madera para que coincida con los parámetros del material de las que sí lo son. Estos resultados muestran cómo los metamateriales mecánicos de madera podrían ayudar a mitigar la variabilidad intrínseca de la madera y la escasez de madera tradicionales.

OPTIMIZATION OF THE ANISOTROPIC ELASTIC PROPERTIES OF A MECHANICAL METAMATERIAL FOR THE DESIGN OF WOODEN MUSICAL INSTRUMENTS.

Guitar-makers have always dealt with wood material variability, since two plates cut from the same log could have very different acoustical behavior. Additionally, global warming is shrinking the habitat of traditional instrument woods (e.g., Engelmann spruce), leading to scarcity and higher manufacturing cost. Both facts have inspired research in alternative materials. In this thesis, we propose wooden mechanical metamaterials as a novel material for instrument-making, whose geometry consists in hole patterns. We studied the effect of pattern variations in the main elastic properties of the metamaterial in the longitudinal and radial directions, namely E_L and E_R. We discovered that the size and symmetry of the holes, as well as the hole size distribution, directly influence those parameters and it is possible to tune them independently or both at the same time. Finally, we developed an optimization algorithm to find the best pattern for fixed target parameters, and we successfully applied the algorithm in cases that resemble both difficulties that inspired this investigation. We showed that wooden mechanical metamaterials can improve the response of wood naturally not well-suited for instruments, carving the wood to match the material parameters of well-suited ones. These results shows how wooden mechanical metamaterials could help to mitigate wood material variability and tonewood scarcity.

El placer del momento antepongamos
a la absurda cura del futuro, cuya
única certeza es el mal presente
con el que compramos su bien.

Ricardo Reis

Agradecimientos

Primero que todo, quiero dedicar esta tesis y agradecer a mi madre, Nadima Chacra, por todo lo que ha hecho por mi desde siempre. Me has enseñado las cosas más importantes en mi vida, muchas gracias por acompañarme en cada paso y formarme como una buena persona, crítica, inteligente, abierta de mente, empática y responsable. Nada de esto podría haber ocurrido sin ti.

Quiero agradecer a mi polola, Berni Ried, por el cariño infinito que me ha entregado estos años. Muchas gracias por caminar conmigo: el cariño y el apoyo durante estos años de pandemia fue crucial.

A mis amigues: Amaranta Tobar, Cristian Saavedra, Francisco Vásquez, Gonzalo Aguilar, Ignacio Hoffmann, y mis K de la E —en especial a Alfredo Habash, Alonso Durán, Bastián Elgueta, Constanza Rivera, Ignasi Neira, José Pedro Jerez y Yazmín Sabat. Les nombraría a todes pero me faltarían páginas para tanto nombre y cariño—. Sin ustedes hubiera sido imposible toda mi experiencia universitaria, muchas gracias por el cariño y el apoyo.

A mis profesores guías Axel Osses y Jean-Gabriel Minonzio, muchas gracias por darme la oportunidad de investigar en algo que me apasiona y dejar fluir mi curiosidad por la matemática en relación con la música. A Carolina Espinoza y Sebastián González, muchas gracias por permitirme colaborar en su investigación, la música, las pizzas, y la buena onda. Me enseñaron mucho sobre la vida, la academia y el trabajo interdisciplinario; agradezco mucho que se hayan dado el tiempo de conversar conmigo y compartir sus experiencias.

Quisiera agradecer también a algunes profesores que fueron muy importantes en mi tiempo en la universidad. A Jocelyn Dunstan por aceptar ser parte de mi comisión, por tu buena disposición y apoyarme cada vez que tuve una duda o ganas de trabajar. Además agradecer a Francisco Förster, Claudio Muñoz, Alejandro Maass y Jaime San Martín; muchas gracias por creer en mi y darme oportunidades que considero invaluables.

No podría dejar fuera a todes quienes forman el DIM: compañeros, administrativas y administrativos. Cultivan un espacio muy agradable para sobrellevar las adversidades de la vida universitaria, y gracias a ustedes pude sentirme acogido cada día. Además quiero agradecer a Catalina Sandoval de Armadillo Lab por sus fructíferas tutorías en escritura académica.

Finalmente, agradezco también a toda la gente que fue importante para mi junto a la que ya no camino. Si alguna vez leen esto, les agradezco mucho el cariño que me entregaron, las experiencias vividas y todo lo que aprendí con ustedes. Tendrán siempre un lugar en mi corazón.

Table of content

List of tables

List of figures

Chapter 1

Introduction

Two problems have existed throughout the entire history of guitar manufacturing. On one hand, wood shows great material variability [1, 2], so even if two guitars are made from the same tree, with the same geometry and manufactured with exactly the same techniques, they will sound different. On the other, climate change has altered the habitat of trees [3, 4], causing wood shortage and making it harder and more expensive for guitar makers to find wood for guitars. This wood scarcity has lead iconic manufacturers to move away from traditional and better suited woods or using them just for premium quality instruments [5]. These difficulties have inspired the research in novel materials to reduce the variability and find ways to tackle climate change using sustainable methods for manufacturing.

Materials such as carbon fiber [6, 7, 8]; Lyrachord, developed by Ovation Guitars [8]; and Ekoa, a composite made of linen fibers and bio-based resins developed by Blackbird [9] are some examples of novel materials used in guitar making. All of them decrease material variations, but they may be expensive to manufacture or not sustainable because they belong to the oil supply chain. Nevertheless, classical guitars have been made with wood since their origins, and the tone associated with wooden instruments is considered the most pleasing. Therefore, as none of these examples is based in wood a lot of effort is put to make the instruments sound with a similar tone to wooden guitars.

Faced with the difficulties of guitar-making and of the materials listed above, wooden mechanical metamaterials arise as a good alternative for the guitar's soundboard, environmentally friendly and more accessible to luthiers (i.e., guitar or instrument makers). Metamaterials are rationally designed materials with non-intuitive mechanical properties based on their structure rather than on the properties of their material composition. Changing the structure of the material it is possible to tune the mechanical parameters [10] and frequency response, introducing the possibility of adapting (or improving) wood for desirable applications.

Guitar-making is one of those applications, since the role of the soundboard mechanical parameters is crucial in the final tone of the instrument. Metamaterials could help reducing the intrinsic material variations or enhancing desired properties for the instruments. However, to the best of our knowledge, only two investigations have applied metamaterials in the realm of instrument making: Oñate et al. [11] have shown that a mechanical metamaterial can modify the power spectrum of a guitar top when glued to it, while Bader et al. [12] attached a ring of masses to the drum membrane resulting in cloaking behavior.

The aim of this thesis is to study the effect of geometric and density variations in the elastic parameters of a wooden mechanical metamaterial consisting on a wooden plate divided in squared cells with a parametrized elliptic hole. First, we explore plates in which all cells share the same parameters. Then, we expand the parameter space dividing the plate in various subsets of cells with different holes to contrast the variations found in the first place with heterogeneous configurations. Finally, an algorithmic optimizations is proposed to find geometries better suited for different needs. This procedure allows to match desired elastic properties or to maximize or minimize related quantities that measure the quality of the wood.

To obtain the elastic constants, we solved the linear elasticity eigenvalue problem for each plate with free boundary conditions and we used the formulas proposed by Caldersmith [13] to relate the Young's Moduli with particular resonance frequencies. All our simulations were realized with FEM tools via the Structural Mechanics module of the commercial software COMSOL. The algorithmic optimization was implemented in the programming language Python, using the numpy package for numerical calculations and mph package as a bridge between COMSOL and Python.

This thesis is organized as follows: Chapter 2 introduces briefly the concepts of double top guitars and wooden mechanical metamaterials. It also gives a review of the mathematical tools of the linearized theory of elasticity and its eigenvalue problems for orthotropic materials. Chapter 3 describes the research objectives and the methodology behind the simulations. Chapters 4 and 5 provide the results for the homogeneous and heterogeneous studies. Even though all the results are shown with the same plate and wood type, consistency tests were made to quantify the variations for different woods and plate size, see Annexes. Finally, chapter 6 describes the algorithmic optimization with successful results..

Chapter 2

Literature review

In this chapter we present a brief review on the topics of guitar-making, metamaterials and the theory of elasticity. First, we show how guitars have evolved through changes in its geometry, modifying its acoustical and mechanical behavior. Then we explain the concept of mechanical metamaterials mainly based in a review written by Yu [10] and show how our investigation is inspired by them. Finally, we introduce the theory of elasticity and other mathematical tools in the special case of wooden plates and their modal study.

2.1. Guitar-making development

While the origins of the guitar can be traced back to its African, Arabic, Asian, and Greek ancestors [14] (See Figure 2.1 for examples of such instruments), Antonio de Torres in the mid 19th century is commonly cited as the first to build the modern guitar as we know it [15, 14], inspired by designs of Sanguino, Pagés, and Alonso [16]. A detailed description of the guitar's anatomy can be found in Figure 2.2. Torres considered the guitar soundboard as the most critical component, so he focused on improving older soundboard building techniques. His instruments had larger lower bouts, incorporated seven radial fan struts and curved lower bout using a *solera* to assemble the guitars [15].

Inspired by successful Torre's designs, many guitar makers from the early 20th century introduced their own modifications to the soundboard, aiming for stronger structures or better tonal balance. For example, Santos Hernández altered the angle of the lower harmonic bar, Herman Hauser varied the height of the struts, and Ignacio Fleta built nine strut guitars with an additional diagonal harmonic bar [15]. Nevertheless, innovations were not only introduced in the structure but new woods started to be used for guitar construction. European Spruce was the main wood used for soundboards in that time, because its light weight and great strength made it well-suited for the application. Despite this, Fleta popularized the use of Western Red Cedar for soundboards, and its guitars with that wood were known for their "Fleta sound" [15].

Figure 2.1: Examples of plucked string instruments, ancestors of the modern guitar. From left to right: drone lute ramsagar, Bina, Delhi, India; 'ud, Tangier, Morocco (II 58); pipa, China (VII 92); sanxian, China (II 26) [14].

Our investigation will be focused in *"Double-top guitars"*, introduced by German guitar-makers Gernot Wagner and Matthias Dammann in the late 1990. Double top guitars arose as a solution to improve the soundboard performance using an aramid polymer related to nylon called *Nomex*. It consists in building the soundboard with two wooden layers (called veneers) with a Nomex Honeycomb core in between, attached with synthetic glue and glued in vacuum [17, 18]. This sandwich board has the benefit of increasing the overall stiffness of the soundboard while decreasing its weight, effectively improving its stiffness to weight ratio.
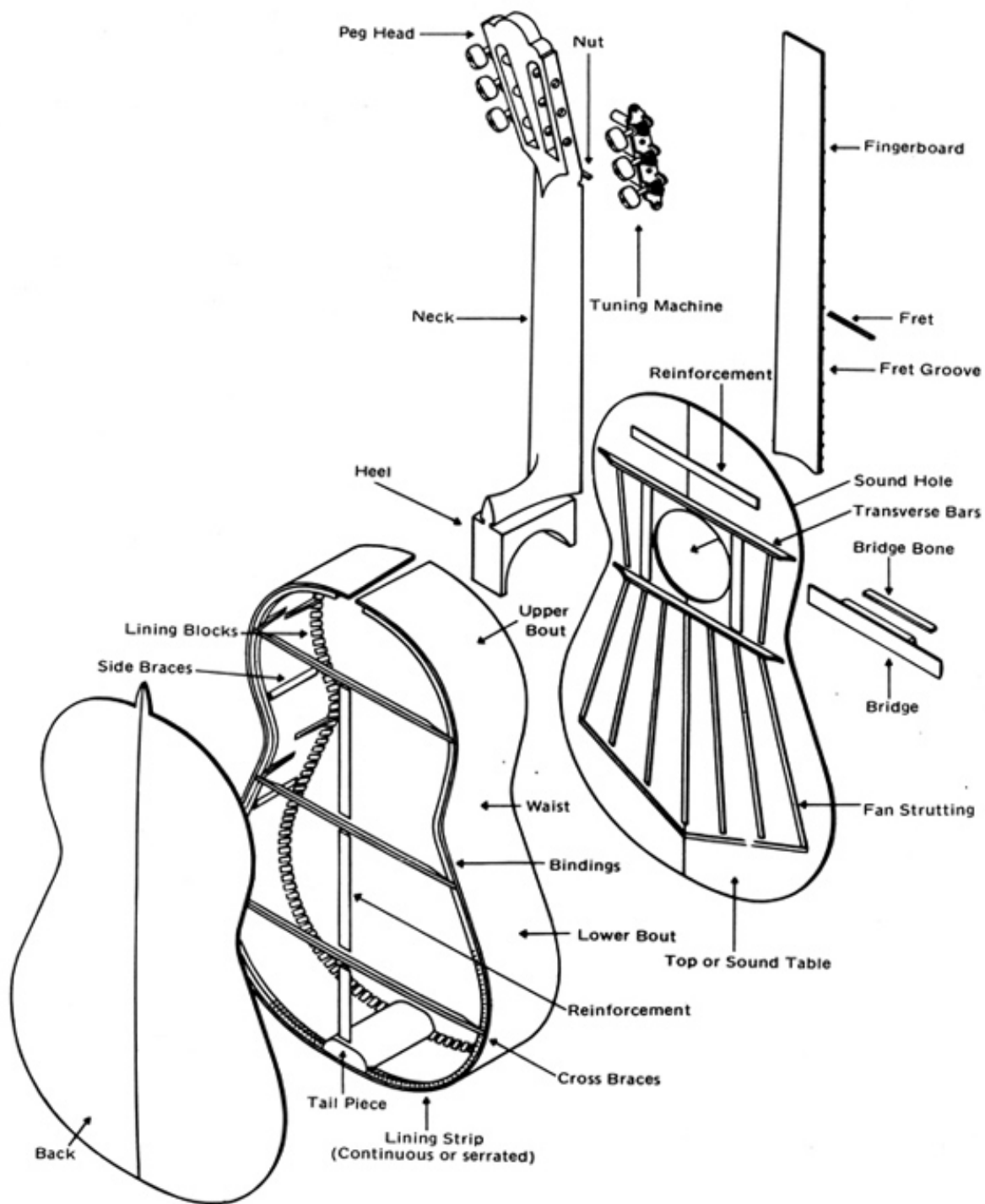
Figure 2.2: Guitar's anatomy [19]. The soundboard (also called Top or Sound Table) shows the fan strutting built by Antonio de Torres. Our research is focused in the acoustic behavior of the wood plate from which the soundboard is made.

Despite these benefits, an additional problem is introduced when using a Nomex Core: the change in materials modifies the soundboard's acoustic impedance, decreasing the acoustic flow between each layer. In addition, there is no consensus on the choice of the core layer's pattern, since guitar makers decide based on a trial and error fashion. Using wood as the

core material could improve the acoustic response of the plate, and studies of the effects of different types of patterns can be made both numerically and experimentally using CNC or laser cutting techniques.

(a) Nomex core with the upper board.

(b) An example of a finished double top soundboard. It is possible to observe the Nomex core between the two layers of wood.

Figure 2.3: Illustration of double top soundboards, courtesy of [20].

All the modifications presented above were partially inspired to improve two important characteristics on guitar soundboards. On the one hand, stronger plates (i.e., higher stiffness) are desired to support string tension. On the other, lighter plates (i.e., lower density) radiate more sound from the instrument, increasing its volume. By changing the number and the height of struts, the number and angle of the harmonic bars, or the nature of the soundboard material, guitar makers have enhanced one or both of these properties. However, their modifications are based solely on their intuition, experience working with wood, and trial and error.

The contribution of science to the realm of instrument-making could help luthiers to choose how to build their instruments in a more informed way, knowing precisely how each modification influences stiffness, density, or acoustic behavior. In addition, the process of choosing the right material or design can help to reduce the material usage and waste induced by trial and an error and prototype constructions. The latter is critical in a world where better suited wood are becoming harder to find due to climate and economical factors [3, 4], so the development of scientific and cost-effective approaches is becoming more and more urgent.

In recent years, scientific approaches to instrument-making have emerged with two general goals. First, validation of luthiers' decisions has been made, for example, in the choices of wood [21, 22], the aging of wood [23], and the bracing effectiveness [24]. The second goal has been to propose new modifications to the guitar structure and building methods, as a way to improve sound or reduce deforestation. For instance, thermal [25] and chemical [26] treatments of wood, new materials such as fiber glass and epoxy [27], and data driven methods of construction [28]. These works have proved the usefulness of scientific studies in instrument-making and how luthiers and companies can benefited with these collaborations.

2.2. Mechanical metamaterials

Metamaterials differ from usual composites in that their properties rely heavily on the topographical optimization in which the designs are based, rather than in the materials of which it is composed [10]. The concept emerged in the field of optics [29, 30, 31], but quickly after researchers expanded the techniques to develop metamaterials in the realm of acoustics and mechanics [32, 33]. Investigations searched and founded materials which can be used as waveguides [34], imperceptibility cloaks [35], and lightweight low frequency sound dampers [36], effectively expanding the behavior found in optics to mechanical and acoustical applications.

Mechanical metamaterials inspire our investigation. This specific type of metamaterials shows unconventional mechanical properties [37, 38, 39, 40], derived from their optimized structure. The geometries are commonly based on periodic structures around a unit cell (See for example Figure 2.4), but non-periodic structures has also been studied [41]. Periodic and non-periodic designs were used during this investigation, in order to compare the benefits and limitations of both. Mechanical metamaterials have been used in biomedical, acoustics, aerospace, and thermal management applications. [42].

We are interested in a particular type of mechanical metamaterial associated with strength and lightweight. These subclass consists of lightweight structures which are adequately stiff and strong, a characteristic that moves them apart from conventional materials where a decrease in density bring forth a drastic degradation in the mechanical properties [10]. Examples of these structures are microlattices, chiral, and hierarchical metamaterials as the ones depicted in Figure 2.4. This group of metamaterials have the exact property we search when building guitar soundboards, so clearly inspiration emerge from these designs.
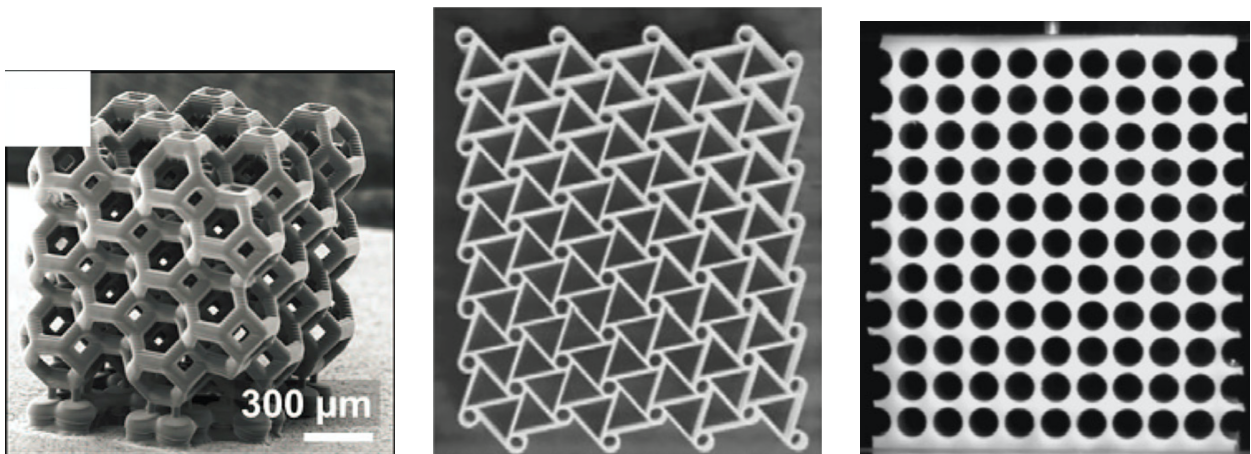
(a) Tetrakaidecahedron unit cell packed into a cubic bend-dominated lattice (Kelvin foam). This structure shows ultra high stiffness-to-density ratio [43]

(b) Tesselation obtained from a hexachiral system. These design form auxectic materials (i.e., negative Poisson's ratios) [44].

(c) Holy sheet. Compressing the material changes its mechanical properties [37].

Figure 2.4: Examples of mechanical metamaterials associated with strength and lightweight.

While the use of materials such as foam, epoxy and all kind of polymers and man-made materials is predominant, wood has been present in both structural [45] and acoustical [46, 47] applications (See Figure 2.5 for images of wooden metamaterials), and even urban trees planted in periodic arrangements can be understood as natural metamaterials used to reduce ground vibrations [48]. Given the importance of acoustics and mechanics in musical instruments a connection between them and metamaterials would seem evident. Moreover, as wood is the fundamental ingredient of many musical instruments, applying wooden metamaterial designs in their construction could solve many of the problems luthiers have found.

(a) Sonic crystals made of resonating bamboo rods [47].

(b) Acoustic barrier made of cylindrical wooden bars [46].

Figure 2.5: Examples of wooden metamaterials.

To the best of our knowledge, only two works have connected mechanical metamaterials and musical instruments: Oñate et al. [11] have shown that a mechanical metamaterial can modify the power spectrum of a guitar top when glued to it, while Bader et al. [12] attached a ring of masses to the drum membrane resulting in cloaking behavior. Our investigation falls within this area of research, directly applying metamaterial designs to the guitar structure (or any wooden musical instrument with soundboard) to change its acoustic response and mechanical behavior.

2.3. Theory of elasticity for wooden plates

2.3.1. PDE's for the eigenvalue problem

Lets consider a wooden plate $\Omega \subseteq \mathbb{R}^3$, with or without holes. We are interested in finding eigenfrequencies and eigenmodes of the fundamental equations of linearized elastodynamics for a 3D elastic body with free boundary conditions. This problem can be modeled as finding pairs $(\mathbf{u}, \lambda) \in H^1(\Omega; \mathbb{R}^3) \times \mathbb{R}$ such that [49]:

$$
\begin{aligned}
-\nabla \cdot \sigma(\mathbf{u}) &= \lambda \rho(\mathbf{x})\mathbf{u} \quad \text{in } \Omega, \\
\sigma(\mathbf{u}) \cdot \mathbf{n} &= 0 \qquad \quad \text{in } \partial\Omega
\end{aligned}
\tag{2.1}
$$

has no trivial solutions, where $\rho(\mathbf{x}) \in L^\infty(\Omega; \mathbb{R}_+)$ is the mass density, $\sigma(\mathbf{u}) \in L^2(\Omega; \mathbb{S}^3)$ is the stress tensor, $\mathbb{S}^3$ representing the space of real 3×3 symmetric matrices, and $\mathbf{n}$ is the unit outward normal vector to Ω in its boundary. The vector $\mathbf{u} \in H^1(\Omega; \mathbb{R}^3)$ represents the

displacement vector due to the deformation of the domain [50].

The stress-strain relation for linear elasticity can be written as

$$\sigma(\mathbf{u}) = A\varepsilon(\mathbf{u}), \tag{2.2}$$

where the strain tensor $\varepsilon(\mathbf{u})$ is given by:

$$\varepsilon(\mathbf{u}) = \frac{1}{2}\left(\nabla\mathbf{u} + \nabla\mathbf{u}^T\right), \tag{2.3}$$

and A is a fourth order tensor such that [51]:

- $A = (a_{ijkl})_{1 \leq i,j,k,l \leq 3}$ and $a_{ijkl} = a_{klij} = a_{jikl} = a_{ijlk}$.

- $\exists \alpha, \beta > 0$ such that $\alpha\beta \leq 1$ and
$$
\begin{aligned}
A\xi : \xi &\geq \alpha|\xi|^2 \\
A\xi : \xi &\geq \beta|\xi|^2
\end{aligned} \tag{2.4}
$$

for all $\xi \in \mathbb{S}^3$, where : represents the scalar product of $\mathbb{S}^3$.

2.3.2. Existence of solutions

Since $\rho(\mathbf{x}) > 0$ and bounded, the linear operator $Bv := \rho v$ is selfadjoint and positive definite, and all its eigenvalues are real and positive [52]. Consequently, if $\Lambda\mathbf{v} := -\nabla \cdot \sigma(\mathbf{v})$, the eigenvalue problem

$$\Lambda\mathbf{u} = B\mathbf{u} \tag{2.5}$$

has real and positive eigenvalues associated to finite dimensional eigenmodes $(\lambda_n)_{n=1}^\infty$, since Λ is selfadjoint and with compact inverse from $L^2(\Omega, \mathbb{R}^3)$ into $L^2(\Omega, \mathbb{R}^3)$ [53].

As we are solving the eigenvalue problem with free boundary conditions, $\lambda_1 = 0$ is the first eigenvalue and its eigenmodes correspond to the rigid displacements of the domain Ω:

$$\mathrm{Ker}\varepsilon = \{\mathbf{u} \in H^1(\Omega; \mathbb{R}^3) : \varepsilon(\mathbf{u}) = 0\}. \tag{2.6}$$

These eigenmodes are important since every attempt to solve the equation numerically will have them as solutions, but we are not interested in them and they will be ignored. They can be avoided using Dirichlet boundary conditions, but the modes we're really interested into (i.e., the fundamental longitudinal and radial modes as explained in Section 3.5) do not appear when fixing any of the boundaries.

2.3.3. Stress-strain relation for orthotropic materials

The tensor A carries the information about the material mechanical response. Orthotropic materials (such as wood, laminated plastic, and various composite materials) posses three orthogonal planes of material symmetry and three corresponding orthogonal axes called the orthotropic axes [54]. The orthotropic axes are commonly called Longitudinal, Radial and Tangential, and they are denoted L, R, and T respectively. Hence, the material mechanical response is described by 9 constants:

- Three orthotropic moduli of elasticity E_L, E_R, and E_T, which measures the object resistance to being deformed elastically when a stress is applied to it.

- Three orthotropic shear moduli G_{LR}, G_{LT}, and G_{RT}, which measures the material elastic shear stiffness.

- Three Poisson's ratios ν_{LR}, ν_{LT}, and ν_{RT}, which characterizes the strain in the second direction produced by the stress in the first one.

Finally, for orthotropic materials we have that $A = S^{-1}$, where S is called the compliance tensor. Using Voigt notation, S can be written as a 6×6 matrix with the following form:

$$
S = \begin{bmatrix}
\frac{1}{E_L} & -\frac{\nu_{RL}}{E_R} & -\frac{\nu_{TL}}{E_T} & 0 & 0 & 0 \\
-\frac{\nu_{LR}}{E_L} & \frac{1}{E_R} & -\frac{\nu_{TR}}{E_T} & 0 & 0 & 0 \\
-\frac{\nu_{LT}}{E_L} & -\frac{\nu_{RT}}{E_R} & \frac{1}{E_T} & 0 & 0 & 0 \\
0 & 0 & 0 & \frac{1}{G_{RT}} & 0 & 0 \\
0 & 0 & 0 & 0 & \frac{1}{G_{TL}} & 0 \\
0 & 0 & 0 & 0 & 0 & \frac{1}{G_{LR}}
\end{bmatrix},
\tag{2.7}
$$

where, E_i corresponds to the Young's modulus, ν_{ij} the Poisson's ratio and G_{ij} the shear modulus [54].

Chapter 3

Methodology

This chapter explain the research objectives as well as all the information related to the simulation procedures. Furthermore, we explain in detail the plate's geometry and its parametrization, wood used for the simulations, quantities of interest and how to calculate them, and simulation procedures.

3.1. Research objectives

The main research objective is to study the effect of geometric variations on the elastic parameters of a wooden mechanical metamaterial, which consists on a plate divided in squared cells with a parametrized elliptic hole. This objective can be broken into three tasks:

1. Describe the variation in density and elastic parameters produced by changes in size and symmetry of the elliptic hole when all the cells share the same geometry.

2. Describe the variation in elastic parameters produced by geometries with multiple cell types for a fixed density.

3. Develop an optimization algorithm to find the best geometry for a given set of target mechanical parameters.

These goals will demonstrate how wooden mechanical metamaterials can increase wood versatility in the manufacture of musical instruments. In addition, tools will be developed to enable luthiers to choose the geometries best-suited to their specific needs. By improving the response of wood naturally not well-suited for soundboards, it will be possible to augment the wood types used for that task, tackling the scarcity of traditional woods with sustainable solutions that do not lose the nature of wood tonal characteristics.

3.2. Setup

Numerical simulations were performed using rectangular plates of standard guitar dimensions, divided into unit cells composed by a square with a centered elliptic or circular hole (see Figure 3.1 for examples of plates). This type of patterns work as a simple way to introduce asymmetries in the geometry by changing the shape and angle of the ellipses. In addition, we took advantage of the orthotropic nature of the material using patterns that preserve the simmetries of wood. First, we studied homogeneous patterns in which all the unit cells share

the same parameters (hence all the holes have the same shape, Fig. 3.1 (b)). Later, those results were expanded with heterogeneous patterns that preserve symmetries with respect to the L or R axes of the plate, Fig. 3.1 (c).
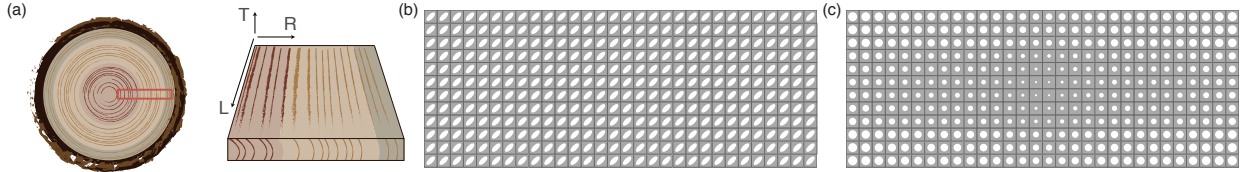
Figure 3.1: Wood cutting scheme (a) Diagram for an orthotropic wood plate and how it is cut from a log: the longitudinal axis L is parallel to the grain, the tangential axis T is tangential to the growth rings and the radial axis R is parallel to the direction of growth of the tree. (b) Top view of a 3D simulated homogeneous plate. (c) Top view of a 3D simulated heterogeneous plate.

We choose Engelmann spruce for the simulations because it is one of the most sought after wood for soundboards. The elastic properties used were taken from Ross et al. [55] and are shown in Table 3.1. In reality spruce's material parameters are not constant, as they could vary depending on the age of the source tree, the plate's location in the log, humidity or absorbed water, among others [1, 56], but for the sake of simplicity we will keep them constant. Even though this might seem arbitrary, we carried simulations with two other types of wood to show that the quantitative change on the effective material parameters is close to independent of the actual values of the wood used (See Annexed C).

Table 3.1: Simulated material properties. The dimensions correspond to the standard plate used for the manufacture of guitar tops: $L \times W \times H = a \times b \times h = 0.6 \times 0.24 \times 0.0035 [m \times m \times m]$. Elastic properties correspond to the ones of Engelmann spruce reported in [55].

Density [kg/m^3]	Young's Moduli [GPa]			Shear Moduli [GPa]			Poissons's Ratios		
ρ	E_L	E_R	E_T	G_{LR}	G_{RT}	G_{LT}	ν_{LR}	ν_{RT}	ν_{LT}
385	8.9	1.13	0.52	1.10	0.09	1.07	0.422	0.530	0.462

3.3.   Quantities of interest

When looking for an ideal wood for guitar's top plates, there are three primary characteristics to consider: the stiffness in the longitudinal direction E_L, the stiffness in the radial direction E_R, and the density of the plate ρ. Besides those three, following Ono [57], the quality of the soundboard can be assessed with two additional acoustical factors: the anisotropy ratio

$$\frac{E_R}{E_L} , \tag{3.1}$$

and the acoustic radiation index, proposed by Schelleng [58], which is the longitudinal sound velocity divided by density:

$$\sqrt{\frac{E_L}{\rho^3}} = \frac{c_L}{\rho} , \tag{3.2}$$

where c_L is the sound velocity (disregarding the Poisson ratio) in the longitudinal direction.

In the case of soundboards, for the first three quantities a suitable wood should have high E_L, low E_R, and low ρ. Besides, low anisotropy ratio and high acoustic radiation are desired. Values for stiffness and density of Engelmann Spruce can be found in Table 3.1, while for the acoustical factors it has nominal values of $E_R/E_L = 0.128$ and $\sqrt{(E_L/\rho^3)} = 12.48 \text{ m}^4/\text{kg·s}$.

These five parameters serve two proposes in this research: to measure the effect of each geometry on the plate's mechanic behavior and to show what configurations are well suited for guitar's top plates. These and other related quantities have been used previously, for example, to measure the effect of ageing [23, 59], the effect of absorbed water [56], and the classification of woods for string instruments [21, 22].

3.4. Parametrization

Every cell is described with a set of three parameters: the volume fraction v of the hole with respect to the unit cell, the aspect ratio k of the elliptic hole, and the angle θ of the hole with respect to the L-axis (See Figure 3.2 for a detailed explanation of the cell parametrization). Hence, if N_r is the number of rows and N_c is the number of columns of cells in the plate, the set of all parameters can be arranged as $\mathcal{P} = \{(v_{ij}, k_{ij}, \theta_{ij})\}_{i=1,\ldots,N_r,j=1,\ldots,N_c}$, counting from left to right and top to bottom. Additionally we defined the void matrix $\mathcal{V} = (v_{ij})_{i=1,\ldots,N_r,j=1,\ldots,N_c}$ as the matrix which contains all the volume fractions of the pattern. All the cells were square shaped, and they shared the same side ℓ. With these parameters we determined the semi-major and semi-minor axes x_i and y_i for each hole:

$$x_{ij} = \sqrt{\frac{\ell^2 v_{ij} k_{ij}}{\pi}} \quad , \quad y_{ij} = \frac{x_{ij}}{k_{ij}} \ , \ i = 1, \ldots, N_r \ , \ j = 1, \ldots, N_c. \tag{3.3}$$

We established two bounds that serve different purposes in the construction of the real wooden plates:

$$k_{ij} < \frac{\pi}{v_{ij}} \left(0.5 - \frac{\delta_1}{\ell}\right)^2 \ , \ i = 1, \ldots, N_r \ , \ j = 1, \ldots, N_c \tag{3.4}$$

and

$$k_{ij} < \frac{v_{ij}}{\pi} \left(\frac{\ell}{\delta_2}\right)^2 \ , \ i = 1, \ldots, N_r \ , \ j = 1, \ldots, N_c \tag{3.5}$$

Equation (3.4) ensures there is at least δ_1 [m] between the boundary of the hole and the outer boundary of the unit cell to keep enough material so that the plate is not too fragile. In addition , Equation (3.5) refers to restrictions of the cutting technique where it is impossible to make holes with one of the semi-axes smaller than δ_2 [m]. During the course of this thesis we used $\delta_1 = \delta_2 = 0.001$, but in practices both values could be different.
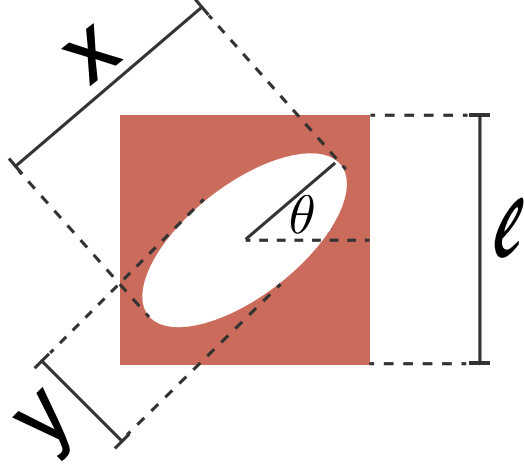
Figure 3.2: Cell parametrization diagram. We define cells of side ℓ with an elliptical hole which shape is controlled with three parameters: the volume fraction with respect to the whole cell $v = \pi xy/\ell^2$, the aspect ratio $k = x/y$ where x and y are the semi-major and semi-minor axes respectively, and the angle θ of the ellipse with respect to the L-axis. In this example we use $(v, k, \theta) = (0.25, 2.2, \pi/4)$.

3.5.   Formulas for effective properties

The three chosen parameters allow us to calculate the effective mechanical properties described in Section 3.3. The effective density is calculated as

$$\rho' = \rho(1 - \overline{V}) \ . \tag{3.6}$$

where $\overline{V}$ is the mean of the void matrix $\mathcal{V}$,

$$\overline{V} = \text{mean}(\mathcal{V}) = \frac{1}{N_r N_c} \sum_{i=1}^{N_r} \sum_{j=1}^{N_c} v_{ij} \tag{3.7}$$

Equation 3.6 has two clear consequences. If we increase $\overline{V}$, the effective density will decrease linearly and the volume fraction is the only parameter that changes the value of ρ'. Taking the latter into account, we will refer to changes in effective density rather than in volume fraction when discussing the results, since ρ' allows a more direct interpretation of the effect of the geometry in the plate's mechanical behavior.

To compute the Young's moduli E'_L and E'_R of the plates we used the formulas proposed in [60, 13]. Namely,

$$\begin{aligned} E'_L &= 12 \times 0.08006 \ \rho' \ a^4 f_{0,2}^2/h^2 \ , \\ E'_R &= 12 \times 0.08006 \ \rho' \ b^4 f_{2,0}^2/h^2 \ , \end{aligned} \tag{3.8}$$

where $f_{0,2}$ is the frequency of the fundamental longitudinal mode (long grain mode), $f_{2,0}$ is the frequency of the fundamental radial mode (cross grain mode) (See Figure 3.3 for an example of the mode shapes), and the constants a, b and h are the dimensions on the longitudinal, radial and transverse direction of the plate described in Figure 3.1. The effect of the Poisson's

ratios are less relevant in the behavior of the instrument [61] so we have disregarded their analysis in what follows.

(a) Fundamental longitudinal mode, $(0, 2)$.

(b) Fundamental radial mode, $(2, 0)$.
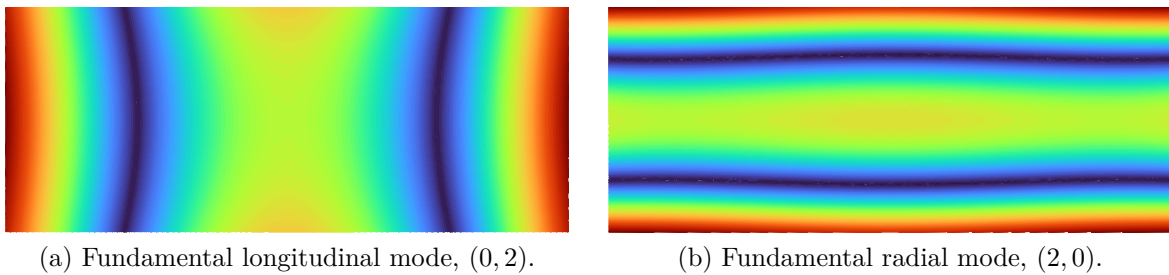
Figure 3.3: Modes used to calculate the desired Young's Moduli. The fundamental longitudinal mode is associated with E'_L, while the fundamental radial mode is associated with E'_R

Because of equations 3.8 are defined for rectangular plates without holes, we test the usefulness of this equation for our patterned plates with numerical tensile tests on different plates, with and without holes, obtaining the longitudinal and radial stiffness (E^t_L and E^t_R, respectively). The relationship between the elastic moduli obtained from the tensile tests and (3.8) was fitted as $E^t_i = \alpha_i E'_i$. For longitudinal stiffness we obtained $\alpha_L = 0.91 \pm 0.04$ with $R^2 = 0.96$. For radial stiffness we obtained $\alpha_R = 0.73 \pm 0.03$ with $R^2 = 0.78$. This means that the longitudinal stiffness is better approximated than the radial stiffness in our perforated plates. Despite these discrepancies, we decided to work with (3.8) instead of tensile tests because it is the method preferred by luthiers. It is important to keep in mind, however, that in both cases the stiffness obtained using (3.8) are smaller than the real yet linearly related ones, but our results remain qualitatively valid with either way of measuring the stiffness.

3.6. Simulation procedures

To obtain the frequencies of the fundamental longitudinal and radial modes, $f_{0,2}$ and $f_{2,0}$, we numerically solve the eigenvalue problem with free boundary conditions related to each wooden plate described. Numerical simulations were performed using the Structural Mechanics module of the commercial software COMSOL, defining the domain, equation and solver. In addition, Python's *mph* package [62] is used as an interface to run COMSOL scripts through Python for the iterative processes to obtain the data, plotting and to implement the final optimization algorithm.

Chapter 4

Homogeneous study

In this chapter results for simulations of homogeneous geometries will be presented. We started by studying the role of the effective density ρ' by simulating circular hole patterns of different radii. Then, we measured the effect of asymmetry using elliptic holes varying their aspect ratio. Finally, we characterized the change of the elastic constants by varying the angle of the ellipses with respect to the longitudinal axis.

4.1. Building homogeneous patterns

By homogeneous pattern we understand plates which share the same parameter for each unit cell. Consequently, $\mathcal{P}_{ij} = (v_{ij}, k_{ij}, \theta_{ij}) = (v^*, k^*, \theta^*) \forall i = 1, \ldots, N_r, j = 1, \ldots, N_c$. By means of the three main parameters (v^*, k^*, θ^*) we changed the hole geometry for every cell. Figure 4.1 shows two examples of plates built with homogeneous patterns.

(a) $(v^*, k^*, \theta^*) = (0.15, 1, 0)$.
(b) $(v^*, k^*, \theta^*) = (0.20, 2, \frac{\pi}{4})$.
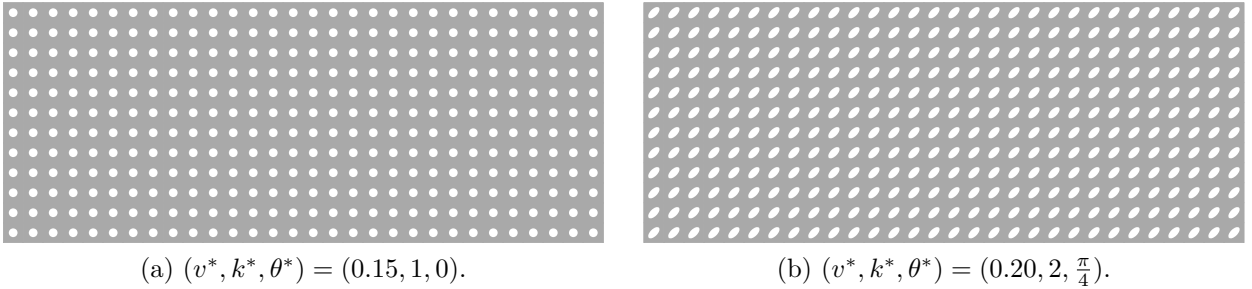
Figure 4.1: Examples for homogeneous patterns.

4.2. Effect of the volume fraction v

To test the effect of the volume fraction in the effective parameters we study the variation caused by increasing the size of circular hole. i.e., increasing the volume fraction and decreasing the effective density. Figure 4.2 shows the variation in the quantities of interest caused by different sizes of circles. Young's Moduli increase as we decrease the circle size. The experiments show a maximum decrease of $78\,\%$ in the longitudinal direction and $76\,\%$ in the radial direction, reaching 1.96 [GPa] and 0.27 [GPa] respectively.

Consequently, both the anisotropy ratio and the acoustic radiation show an increase of 14 % and 85 % over the original value. The anisotropy ratio shows a maximum value of 0.146 while the acoustic radiation reaches 23.13 [m⁴/kg·s]. However, while the acoustic radiation shows a monotonous increase when we increase the volume fraction, the value of the anisotropy ratio does not depend on changes of the volume fraction and it remains almost constant.
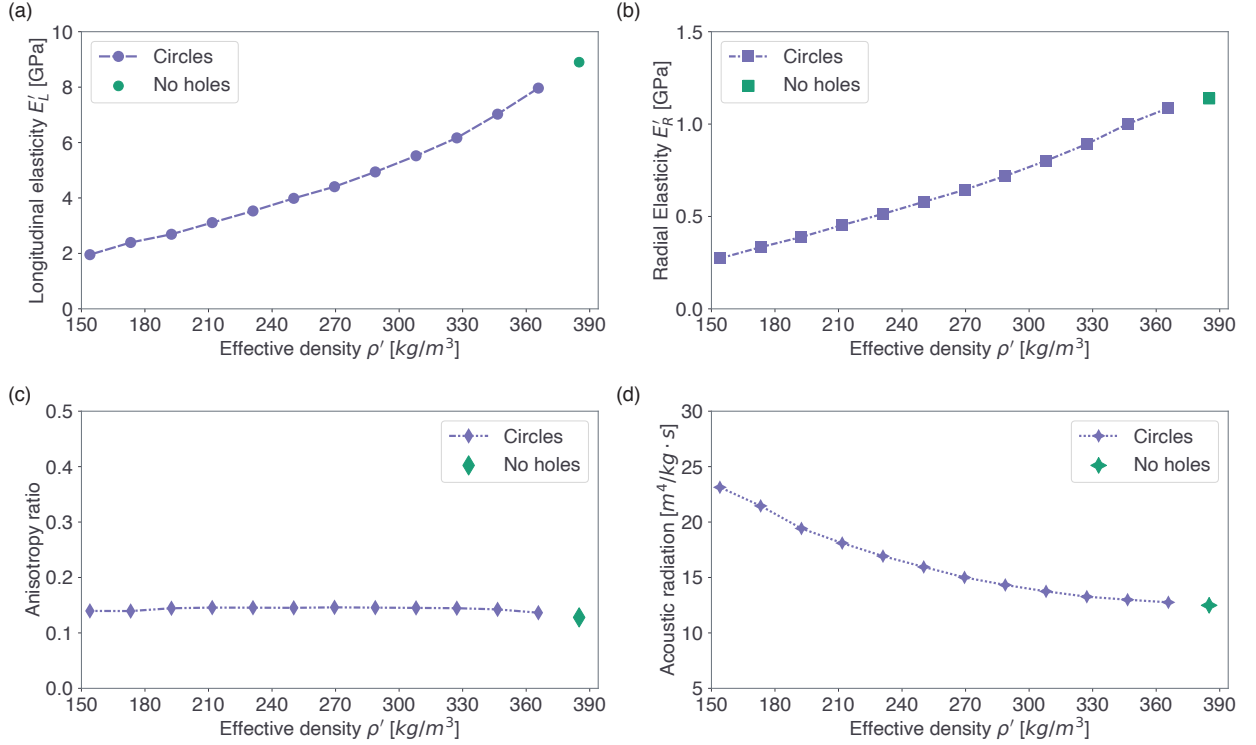
Figure 4.2: Effects of changing the effective density with circular holes of varying size. (a) Longitudinal elasticity. (b) Radial elasticity. (c) Anisotropy ratio. (d) Acoustic radiation damping factor.

4.3.   Effect of the aspect ratio k

By keeping the volume fraction of the hole constant and varying the aspect ratio we can study how the geometry of the hole affects the stiffness. Figure 4.3 shows the behavior of the quantities of interest for different aspect ratios and volume fractions, both for ellipses parallel and perpendicular to the longitudinal axis.

It is remarkable to see that now, in contrast with circular holes, for every volume fraction there is an interval of reachable values instead of just a point, effectively increasing the variation of the elastic parameters. Black points in each of the graphics of Figure 4.3 represent the same values as 4.2, while the arrows show the interval of reachable parameters for both parallel and perpendicular ellipses.

The results show that if we increase the effective density, the range of variation increase. This effect is directly related with the bound introduced in 3.4, because as we decrease the volume fraction the interval of possible aspect ratios increase. It is also possible to see that

even though now there is a range of values for each density, each graphic of Figure 4.3 follow the same overall trend dictated by the change in volume fraction described in Section 4.2.

In numerical terms, the longitudinal stiffness E'_L shows maximum and minimum variation of 81 % and 11 %, reaching 1.72 [GPa] and 7, 96 [GPa] respectively. Additionally, E'_R varies between maximum and minimum variations of 79 % and 3 %, reaching 0.24 [GPa] and 1.10 [GPa].

While with circular holes the anisotropy ratio and acoustic radiation always increase, changing the aspect ratio and orientation it is possible to decrease both values. With ellipses perpendicular to the longitudinal direction the value of E'_R/E'_L increases up to 0.377 with a maximum variation of 195 %. Ellipses parallel to that direction decrease the anisotropy ratio by 46 % with a value of 0.068.

The acoustic radiation changes in the opposite way. Ellipses perpendicular to the longitudinal direction decrease the value by a maximum variation of 38 % at a value of 7.72 [m^4/kg·s]. The value with horizontal ellipses increases up to 95 % at a value of 24.39 [m^4/kg·s].
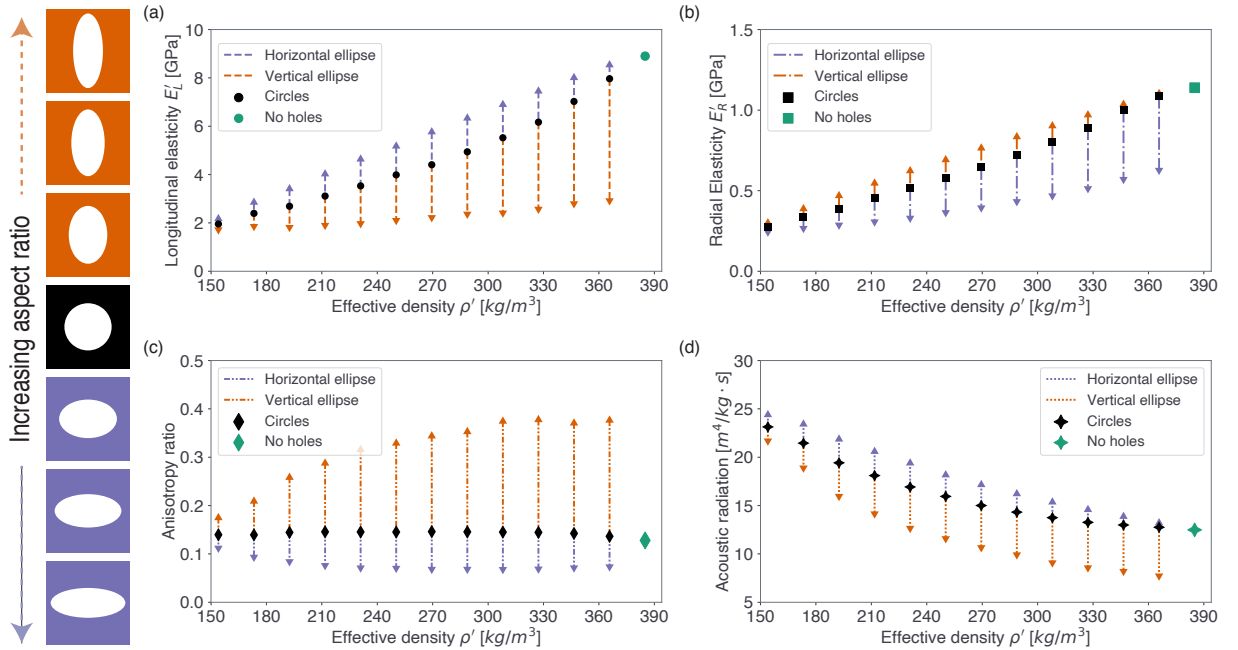
Figure 4.3: Effects of changing the aspect ratio for different effective densities. The cell diagram on the left side shows the meaning of the colors in each vertical line: black is the unit cell with circular hole and the further away from it, the larger the aspect ratio for horizontal (in purple) or vertical (orange) ellipses. (a) Longitudinal elasticity. (b) Radial elasticity. (c) Anisotropy ratio. (d) Acoustic radiation damping factor.

4.4. Effect of the angle variation θ

Now we focus our attention on the dependence of the stiffness and both acoustical factors on the angle with respect to the longitudinal direction at which the ellipse is positioned. Figure 4.4 shows changes of the quantities of interest for three different volumes, each one with the maximum aspect ratio given by the bounds 3.4 and 3.5 , and rotating the ellipses

18

from 0 to π. In contrast with the parameters studied in the previous sections, smooth angle variations produces changes in the shape of some of the studied eigenmodes (See Annexed A for a further discussion in this topic).

All the observables present the same periodicity, which is expected from the symmetry of the unitary cell. It is easy to see that the smaller the hole is, the larger is the range that the stiffness varies when varying the angle, mainly because the bigger the hole the less asymmetry in the geometry, because the maximum aspect ratio decreased significantly. For the case of the anisotropy ratio the variation with the density is not very noticeable, whereas for the acoustic radiation it is inverted: the larger the hole, the more this value changes when varying the angle.

The limits of the intervals in which every quantity varies are the same as in subsection 4.3. This can be understood by noticing that, for every curve, the maximum and minimum are respectively reached when the ellipse is either parallel or perpendicular to the longitudinal direction. However, not the whole range of values is reachable by varying only the angle as can be seen by the 'jump' on the longitudinal stiffness mostly visible for the highest effective density (purple line) in Fig. 4.4 (a).

(a)   (b)

(c)   (d)
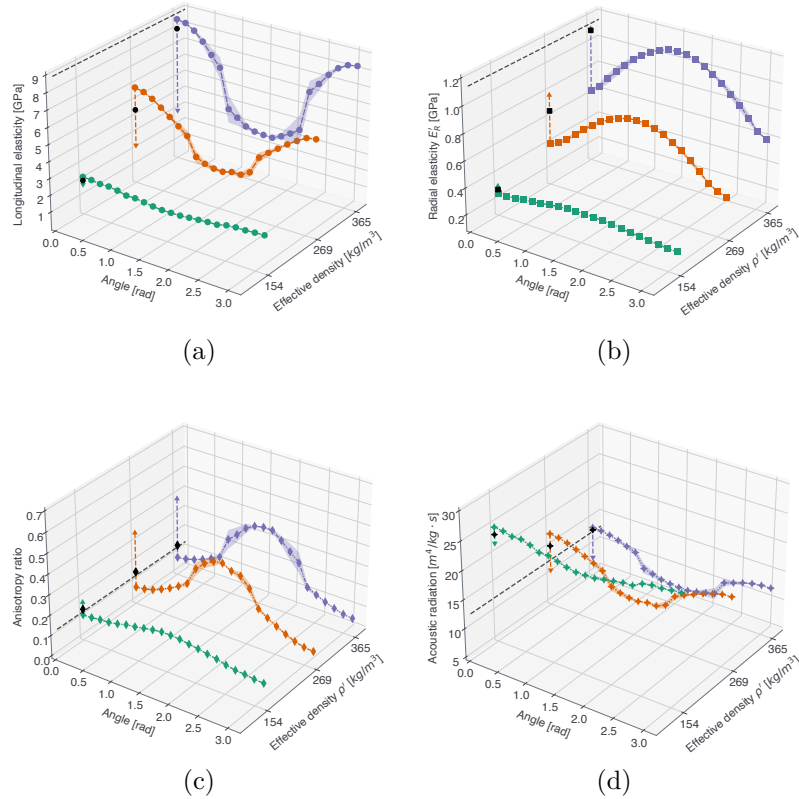
Figure 4.4: Effects of the angle of the ellipse. All the observables present a periodicity on the angle, which is obvious from the symmetry of the shape of the hole. Interestingly though, the variation in the longitudinal direction is much larger than in the radial direction, and both ranges of variation depend heavily on the effective density of the plate: the smaller the hole the larger the range that the stiffness varies when varying the angle. It is possible to see the same behavior for the acoustic radiation. (a) Longitudinal elasticity. (b) Radial elasticity. (c) Anisotropy ratio. (d) Acoustic radiation damping factor.

4.5. Phase plane $E_L - E_R$

It would seem from the previous results that E'_L and E'_R are inversely related: when varying either the aspect ratio or the angle of the ellipses one increases when the other decreases. However, from the measurements of the anisotropy ratio one can see that the variation in each way of modifying the holes is peculiar. To understand this better we plot all the previous results together in a E'_R-E'_L plot where the effects of the geometry is better illustrated.

Figure 4.5 (a) shows the results for some of our simulations in the space of normalized radial and longitudinal stiffness for the plates with aspect ratio variation. Aspect ratio tends to affect only one stiffness at the time: for the case of vertical ellipses, E'_L varies more than E'_R and the opposite occurs for horizontal ellipses. In contrast, the behavior for angle variations is very different (see Figure 4.5 (b)), since it varies both elastic constants at the same time, in a roughly inverse relation.

(a) Aspect ratio variations.　　　　　　　　　　(b) Angle variations.
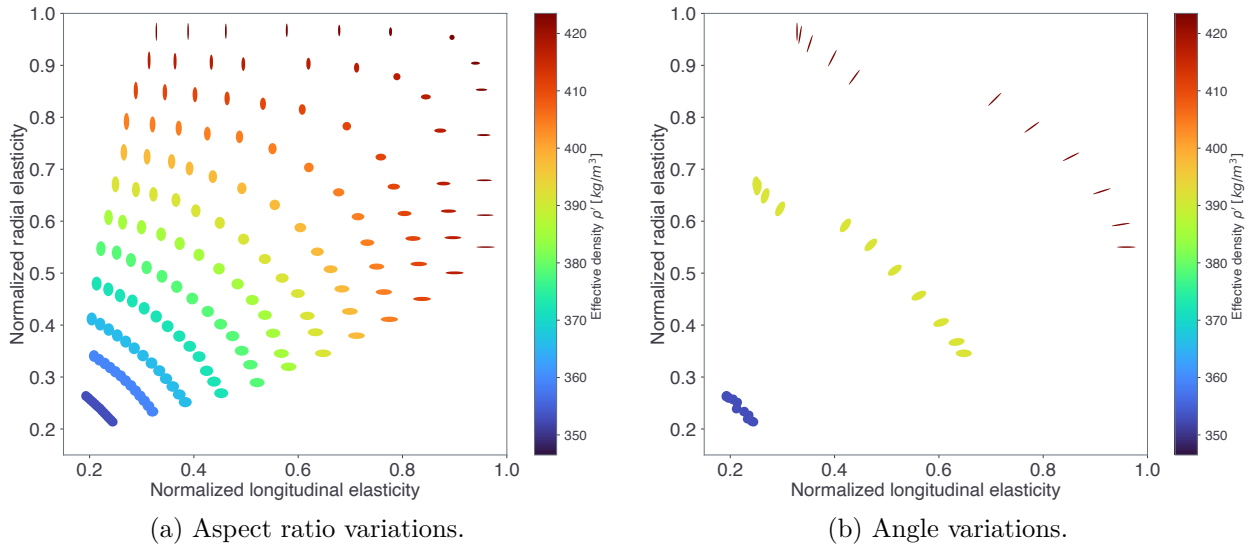
Figure 4.5: Results for plates with (a) aspect ratio variation and (b) angle variation, normalized by Engelmann Spruce elastic parameters. The shape of the point represent the hole shape of the corresponding plate, while the color map represents the associated effective density. For the case of vertical ellipses, E'_L varies more than E'_R and the opposite occurs for horizontal ellipses. Angle variations change both elastic constants at the same time, in a roughly inverse relation.

Chapter 5

Heterogeneous study

In this chapter, results for simulations of heterogeneous geometries will be presented. As we are interested in variations in density, we focus on plates with circular hole patterns with different sizes. We study non-periodic patterns that take advantage of the longitudinal and radial axes of symmetry, allowing us to change the corresponding elastic parameters almost independently.

5.1. Building heterogeneous geometries

By heterogeneous pattern we understand arrays of cells in which the parameters defining them are not shared across the plate. Instead, subsets of cells could have different holes, while in the limit every cell could have independent parameters. We are interested in the effect of density variations in the plate, so only patterns with circular holes will be used in order to avoid the effects of asymmetries in the holes produced by changes in aspect ratio and angle. Hence, for the rest of this chapter we will assume $k_{ij} = 1, \theta_{ij} = 0, \forall i = 1, \ldots, N_r, j = 1, \ldots, N_c$.

5.1.1. Symmetries

We divided the study into two groups: the first group corresponds to geometries symmetric with respect to the R axis, divided by groups of columns with the same parameters. Consequently, this group consists of patterns such that

$$v_{i,j} = v_{i,N_c-(j-1)} = \nu_j^c, \nu_j^c \in [0,1], \forall i = 1, ..., N_r, j = 1, ..., \lfloor \frac{N_c}{2} \rfloor. \tag{5.1}$$

Similarly, the second group takes advantage of L-axis symmetries, so the group consists in patterns such that

$$v_{i,j} = v_{N_r-(i-1),j} = \nu_j^r, \nu_j^r \in [0,1], \forall i = 1, ..., \lfloor \frac{N_r}{2} \rfloor, j = 1, ..., N_c. \tag{5.2}$$

As a consequence, R-symmetric patterns will be described with void vectors $V_c = (\nu_j^c)_{j=1,...,\frac{N_c}{2}} \in$

$[0, 1]^{\frac{N_c}{2}}$ with its associated void matrix $\mathcal{V}_c$, and the L-symmetric ones described by void vectors $V_r = (\nu_j^r)_{i=1,\ldots,\frac{N_r}{2}} \in [0, 1]^{\frac{N_r}{2}}$ with its associated void matrix $\mathcal{V}_r$. We started studying effects in the mechanical parameters of each group (See Section 5.2), and then we combined symmetries (See Section 5.3), keeping the same effective density for each geometry. Figure 5.1 shows examples of plates for both types of symmetries.

(a) R-symmetric pattern.   (b) L-symmetric pattern.
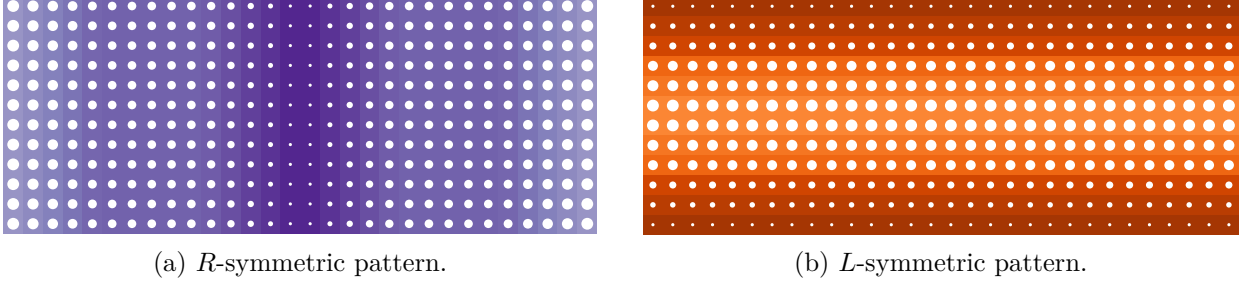
Figure 5.1: Examples for (a) R-symmetric and (b) L-symmetric patterns. The darker the cell the greater the effective density.

5.1.2. Choosing void vectors

We used the following method to build the void vectors for the symmetries described above: first, we fixed an objective mean volume fraction v^* which defines the maximum and minimum void volumes of the plate, v_M and v_m respectively, as:

$$v_M := \begin{cases} 2v^* - 0.02 & \text{if } 2v^* - 0.02 < 0.6 \\ 0.6 & \text{if } 2v^* - 0.02 \geq 0.6 \end{cases} \tag{5.3}$$

$$v_m := \begin{cases} 0.02 & \text{if } 2v^* - 0.02 < 0.6 \\ 2v^* - 0.6 & \text{if } 2v^* - 0.02 \geq 0.6 \end{cases} \tag{5.4}$$

The restrictions imposed in $v_{M,m}$ allow us to build patterns coherent with experimental cutting methods and the restrictions imposed in Section 3.4. Then, taking $\mu \in \mathbb{R}$, we defined the void vectors independently from the type of symmetry as follows: defining $N_{c,r}^* := N_{c,r}/2$,

- If $N_{c,r}^*$ is even, $V_{c,r} = (\nu_k^{c,r})_{k=1,\ldots,N_{c,r}^*}$ is defined by:

$$\nu_k^{c,r} := \begin{cases} v_m + \mu(N_{c,r}^* - k) & \text{if } k > \frac{N_{c,r}^*}{2} \\ v_M - \mu(k - 1) & \text{if } k \leq \frac{N_{c,r}^*}{2} \end{cases} \tag{5.5}$$

- If $N_{c,r}^*$ is odd, $V_{c,r} = (\nu_k^{c,r})_{k=1,\ldots,N_{c,r}^*}$ is defined by:

$$\nu_k^{c,r} := \begin{cases} v_m + \mu(N_{c,r}^* - k) & \text{if } k > \lfloor \frac{N_{c,r}^*}{2} \rfloor \\ v^* & \text{if } k = \lfloor \frac{N_{c,r}^*}{2} \rfloor \\ v_M - \mu(k - 1) & \text{if } k < \lfloor \frac{N_{c,r}^*}{2} \rfloor \end{cases} \tag{5.6}$$

Defining $V_{c,r}$ in this manner ensures that the volumes are in decreasing order, building patterns with big holes near the edges and smaller ones near the center of the plate, as the ones in Figure 5.1. The parameter μ quantifies the steepness of the void gradients: the smaller the μ, the greater the difference in volume fraction (hence, in effective density) between the edges and the center (Compare the patterns from Figure 5.2 with $\mu = 0.04$ with the ones from Figure 5.3 with $\mu = 0.002$). Besides, to keep the vector $V_{c,r}$ in descending order, μ must satisfy the bound

$$\mu \leq \frac{v_M - v_m}{2(\frac{N^*_{c,r}}{2} - 1)} \tag{5.7}$$

To show that patterns built with this method preserve v^*, we prove the equality for the case of R-symmetric patterns and N^*_c even, since the others are analogous: from the way in which the patterns are built, it is clear that

$$\overline{V}_c = \text{mean}(\mathcal{V}_c) = 2N_r \sum_{j=1}^{N^*_c} \nu^c_j \tag{5.8}$$

Hence,

$$\overline{V}_c = \frac{1}{N_r N_c} \sum_{i=1}^{N_r} \sum_{j=1}^{N_c} v_{ij}$$

$$= \frac{1}{N_r N_c} 2N_r \sum_{j=1}^{N^*_c} \nu^c_j \tag{5.9}$$

$$= \frac{1}{N^*_c} \sum_{j=1}^{N^*_c} \nu^c_j$$

Replacing ν^c_j from Equation (5.5),

$$\frac{1}{N^*_c} \sum_{j=1}^{N^*_c} \nu^c_j = \frac{1}{N^*_c} \left(\sum_{j=1}^{N^*_c/2} \nu^c_j + \sum_{k=N^*_c/2+1}^{N^*_c} \nu^c_k \right)$$

$$= \frac{1}{N^*_c} \left(\frac{N^*_c}{2}(v_M + v_m) + \sum_{j=1}^{N^*_c/2} \mu(j-1) - \sum_{k=N^*_c/2+1}^{N^*_c} \mu(N^*_c - k) \right) \tag{5.10}$$

$$= \frac{1}{N^*_c} \left(\frac{N^*_c}{2}(v_M + v_m) + \sum_{\tilde{j}=0}^{N^*_c/2-1} \mu\tilde{j} - \sum_{\tilde{k}=0}^{N^*_c/2-1} \mu\tilde{k} \right)$$

$$= \frac{1}{N^*_c} \frac{N^*_c}{2}(v_M + v_m) = \frac{v_M + v_m}{2} = v^*$$

where the last equality holds because from Equations 5.3 and 5.4 it is clear that $v_M + v_m = 2v^*, \forall v^* \in (0,1)$. Therefore, the objective mean volume fraction is reached.

Finally, we define $\tilde{V}_{c,r} = (\tilde{\nu}^{c,r}_j)_{j=1,\ldots,N^*_{c,r}} := (\nu^{c,r}_{N^*_{c,r}-(j-1)})_{j=1,\ldots,N^*_{c,r}}$ as reverse ordered versions of $V_{c,r}$, with void matrices $\mathcal{V}_{\tilde{c},\tilde{r}}$ respectively. These vectors allow us to built patterns with volume fractions in ascending order, that is, with small holes near the edges and bigger ones near the center of the plate (See Figure 5.2 for examples of plates built with V_c and $\tilde{V}_c$).

(a) V_c, descending order.

(b) $\tilde{V}_c$, ascending order.
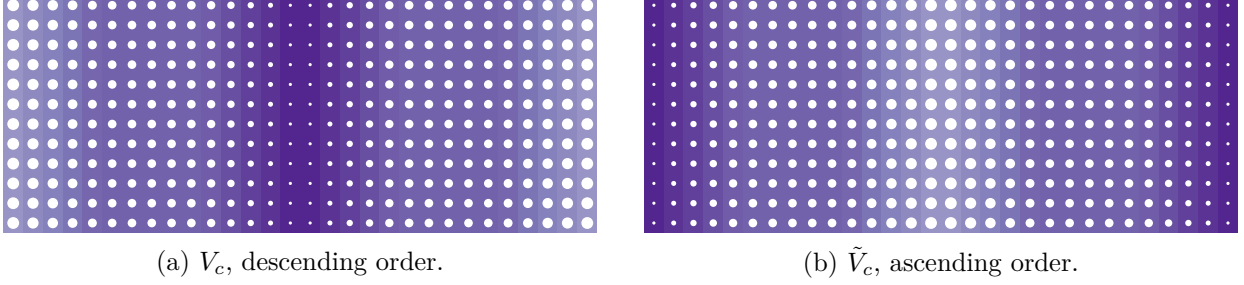
Figure 5.2: Examples of plates built with (a) V_c and (b) $\tilde{V}_c$, taking $v^* = 0.15$ and $\mu = 0.04$. The darker the cell the greater the effective density.

5.2. Results combining patterns with the same symmetry

How the patterns are defined allows us to linearly combine the void matrices to create new geometries, instead of building new matrices every time from the ground up. For $\lambda \in [0, 1]$, we define

$$\mathcal{V}_{c,r}^{\lambda} = \lambda \mathcal{V}_{c,r} + (1 - \lambda)\mathcal{V}_{\tilde{c},\tilde{r}}, \qquad (5.11)$$

and noting that

$$
\begin{aligned}
\overline{V}_{c,r}^{\lambda} = \text{mean}(\mathcal{V}_{c,r}^{\lambda}) &= \frac{1}{N_{c,r}^*} \sum_{j=1}^{N_{c,r}^*} \lambda \nu_j^{c,r} + (1 - \lambda)\tilde{\nu}_j^{c,r} \\
&= \frac{\lambda}{N_{c,r}^*} \sum_{j=1}^{N_{c,r}^*} \nu_j^{c,r} + \frac{1 - \lambda}{N_{c,r}^*} \sum_{k=1}^{N_{c,r}^*} \tilde{\nu}_k^{c,r} \\
&= \lambda v^* + (1 - \lambda)v^* = v^*, \forall \lambda \in [0, 1]
\end{aligned} \qquad (5.12)
$$

it is possible to take convex combinations between void matrices and preserve the same mean volume fraction in the created patterns. This method enables us to study the effect of different volume gradients just by changing the value of λ, instead of changing the value of μ and the vectors $V_{c,r}$.

In particular, when taking $\lambda = \frac{1}{2}$, we can recover an homogeneous pattern in which every cell has the same volume fraction v^*. In fact,

$$
\begin{aligned}
\frac{1}{2}(\nu_k^{c,r} + \tilde{\nu}_k^{c,r}) &= \frac{1}{2}(\nu_k^{c,r} + \nu_{N_{c,r}^*-(k-1)}^{c,r}) \\
&= \frac{v_M + v_m}{2} = v^*, \forall k = 1, ..., N_{c,r}^*
\end{aligned} \qquad (5.13)
$$

Furthermore, when $\lambda < \frac{1}{2}$, the plate presents bigger holes in the center and concentrates the density in the edges, while $\lambda > \frac{1}{2}$ has the opposite effect.

As an example of the changes produced by opposite geometries and their combination, Figure

24

5.3 shows the effect in the elastic parameters of both groups of symmetries for $v^* = 0.15$ and $\mu = 0.002$. The plot at the center of Figure 5.3 (a) shows the normalized values of the elastic parameters for R-symmetric patterns and different values of λ_R. While we see a variation of 41.5% in the value of E'_L, the value of E'_R barely changes with a variation of 1.1%. In contrast, L-symmetric patterns for different values of λ_L (See Figure 5.3 (b)) show greater variability in E'_R with a change in its value of 37.2% while changing the value of E'_L at a maximum of 6.1%.
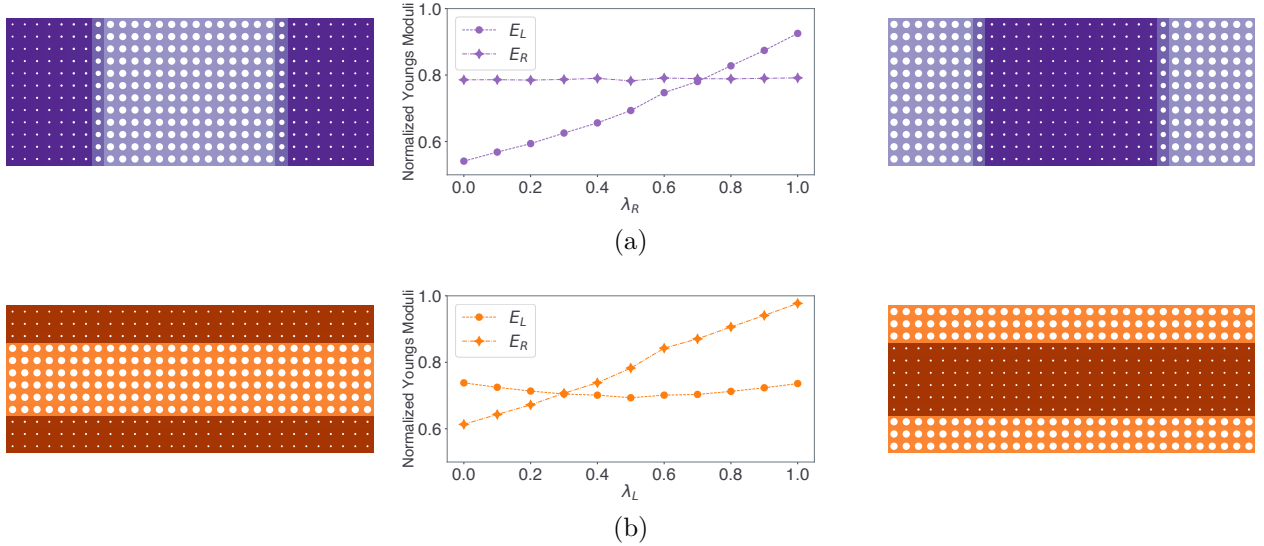
Figure 5.3: Values of the elastic properties for both groups symmetries with $v^* = 0.15$ and $\mu = 0.002$, normalized by Engelmann Spruce elastic parameters. $\lambda_{R,L}$ parametrize the transformation between the pattern on the left ($\lambda_{R,L} = 0$) and the pattern on the right ($\lambda_{R,L} = 1$), passing by different gradients of hole sizes. At $\lambda_{R,L} = 0.5$ we recover an homogeneous configuration. (a) Initial R-symmetric patterns used and elastic parameters for its combinations. While the value of E'_R remains almost constant, E'_L shows great variability when changing the density distribution. (b) Initial L-symmetric patterns used and elastic parameters for its combinations. While the value of E_L barely changes, E_R shows great variability when changing the density distribution.

Figure 5.3 also shows that taking values of $\lambda_{R,L}$ closer to 0.5 (i.e., less pronounced volume gradients or greater values of μ) decreases the difference between the obtained elastic parameters and the ones associated with the homogeneous pattern. Consequently, smaller values of μ in the initial patterns increase the range of possible values that the elastic parameters could take in the combined pattern. However, while it might seem disadvantageous to increase the value of μ, it could be useful to have several patterns that reach the same elastic parameters.

Another way to visualize these results is by studying the $E'_L - E'_R$ plane and how heterogeneous patterns and their combinations move around it. Figure 5.4 (a) shows the effect of combinations of R-symmetric patterns with $v^* = 0.15$, $\mu = 0.002$, and several values of λ_R. Clearly, the E'_R value barely moves, and the value for the homogeneous pattern is reached. Similarly, Figure 5.4 (b) shows that combining L-symmetric patterns with $v^* = 0.15$ and $\mu = 0.002$ varies E'_L much less than E'_R. As a result, we can modify one of the elastic parameters barely modifying the other by choosing the correct pattern symmetry.
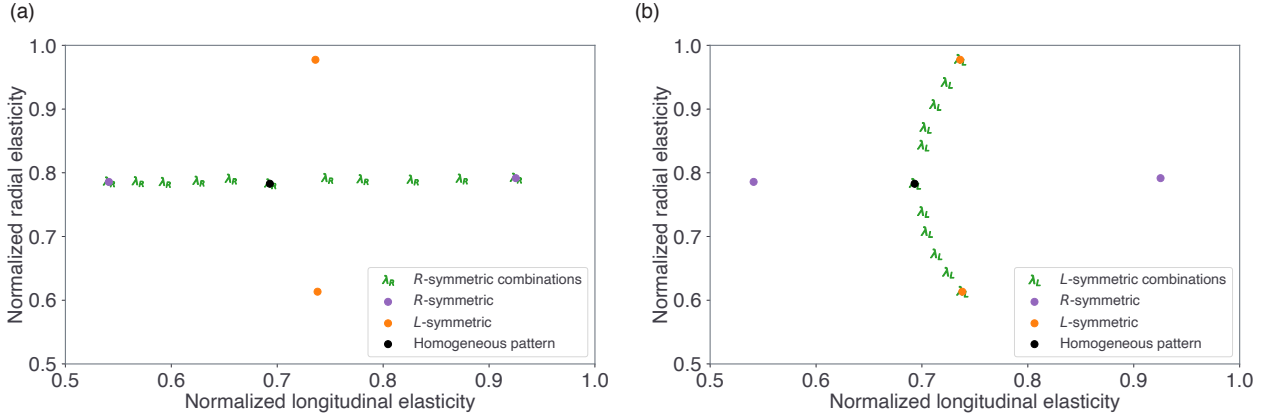
Figure 5.4: $E'_L - E'_R$ plots (normalized by Engelmann Spruce elastic parameters) for patterns with $v^* = 0.15$. Purple and orange values are taken from patterns with $\mu = 0.002$. Both graphics show the values reached by the homogeneous pattern, R-symmetric and L-symmetric configurations without convex combinations. Taking convex combinations it is possible to modify the value of one of the elastic parameters while barely changing the other. (a) Results combining R-symmetric patterns. While the value of E'_R remains almost constant, E'_L shows great variability when changing the density distribution. (b) Results combining L-symmetric patterns. While the value of E'_L barely changes, E'_R shows great variability when changing the density distribution.

To summarize, Figure 5.5 shows the effect of heterogeneous patterns for various effective densities. The figure presents the area of reachable values for E'_L and E'_R for several objective volume fractions v^*, using the same method with $\mu = 0.002$ and varying the values of $\lambda_{L,R}$. For both cases, we compare the new values with the ones reached with homogeneous patterns reported in Chapter 4. Results show that taking heterogeneous configurations it is possible to reach higher values of both elastic parameters —but not at the same time— keeping them really close to the original value with up to 30 % less density.
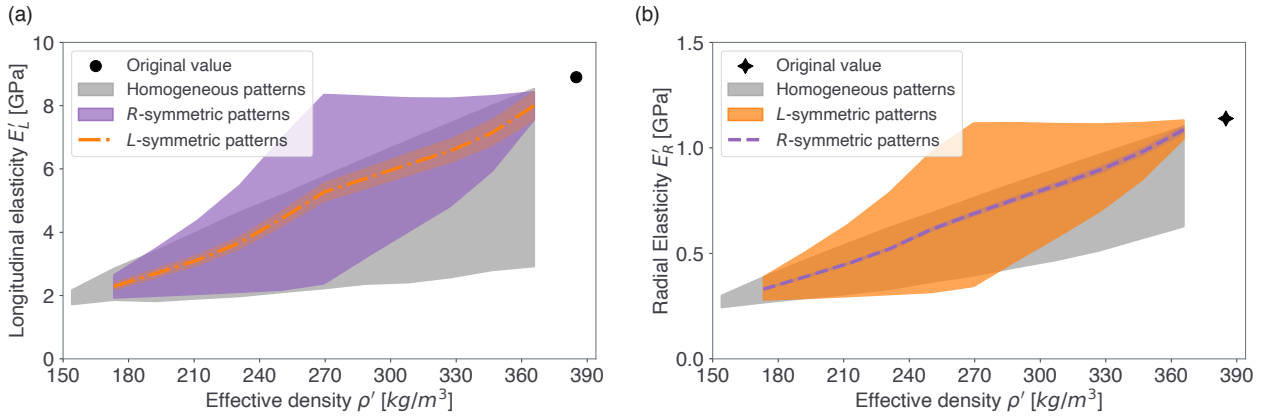
Figure 5.5: Stiffness versus density plots of the elastic parameters E'_L and E'_R. While changing the effective density (i.e., mean volume fraction) allows us to move horizontally, taking different values of $\lambda_{L,R}$ it is possible to move vertically inside the region, for a fixed density. For both parameters we see a direct influence of one of the type of symmetries, while the other keeps the elastic properties almost constant for each effective density. The gray region shows the values obtainable by homogeneous patterns shown in Chapter 4. Notice how it is possible to reach higher values of stiffness for almost any density with heterogeneous configurations than with homogeneous patterns. (a) Longitudinal elasticity E'_L. (b) Radial elasticity E'_R.

The remaining quantities of interest has also been studied for heterogeneous patterns. Figure

5.6 (a) shows the range of values of the Anisotropy ratio for each symmetry. While both types of patterns show variations, none of them reaches the range possible using homogeneous patterns with ellipses. This behavior can be explained because even though we are able to reach higher values of both elastic parameters, the Anisotropy ratio takes into account the difference between them which do not change as much as in the homogeneous case.

The acoustic radiation (See Figure 5.6 (b)) increases its value in several effective densities when using R-symmetric patterns, as these symmetries influence the value of E'_L. Conversely, L-symmetric patterns show a neglectful influence in the Acoustic radiation, because as seen in Figure 5.3 (b) these patterns do not influence the value of E'_L significantly. This behavior makes the Acoustic radiation for L-symmetric patterns stay within the range of values reachable for homogeneous patterns, while R-symmetric patterns reach higher values and variations comparable with the homogeneous case.
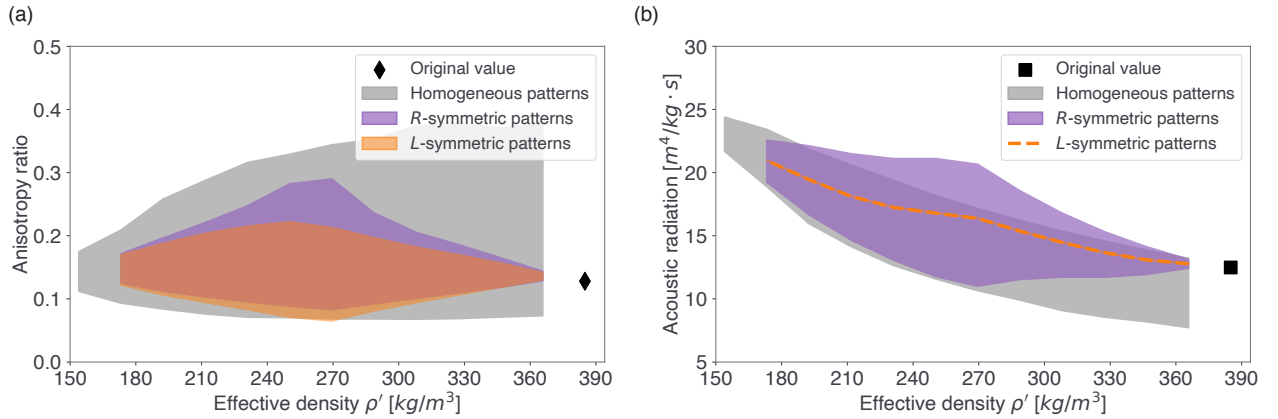
Figure 5.6: Anisotropy ratio versus density and Acoustic radiation versus density plots. While changing the effective density (i.e., mean volume fraction) allows us to move horizontally, taking different values of $\lambda_{L,R}$ it is possible to move vertically inside the region, for a fixed density. (a) Anisotropy ratio. The ratios for heterogeneous do not succeed at reaching lower values than with homogeneous ones. (b) Acoustic radiation. While R-symmetric patterns could reach higher values of radiation for some effective densities, L-symmetric patterns do not show great variation mainly because this type of patterns have little influence in the value of E'_L.

5.3. Results combining patterns with different symmetries

Taking convex combinations between void matrices also enables us to combine patterns with different symmetries, defining

$$\mathcal{V}_{(\lambda_c,\lambda_{\tilde{c}},\lambda_r,\lambda_{\tilde{r}})} := \lambda_c \mathcal{V}_c + \lambda_{\tilde{c}} \mathcal{V}_{\tilde{c}} + \lambda_r \mathcal{V}_r + \lambda_{\tilde{r}} \mathcal{V}_{\tilde{r}}, \tag{5.14}$$

where

$$(\lambda_c, \lambda_{\tilde{c}}, \lambda_r, \lambda_{\tilde{r}}) \in [0,1]^4 \text{ such that } \lambda_c + \lambda_{\tilde{c}} + \lambda_r + \lambda_{\tilde{r}} = 1. \tag{5.15}$$

Using the patterns defined in the previous section it is possible to obtain new density distributions, like the ones depicted in Figure 5.7.

As in the previous section, $\mathcal{V}_{(\lambda_c, \lambda_{\tilde{c}}, \lambda_r, \lambda_{\tilde{r}})}$ preserves v^*, since

$$\text{mean}(\mathcal{V}_{(\lambda_c, \lambda_{\tilde{c}}, \lambda_r, \lambda_{\tilde{r}})}) = \lambda_c\text{mean}(\mathcal{V}_c) + \lambda_{\tilde{c}}\text{mean}(\mathcal{V}_{\tilde{c}}) + \lambda_r\text{mean}(\mathcal{V}_r) + \lambda_{\tilde{r}}\text{mean}(\mathcal{V}_{\tilde{r}})$$
$$= (\lambda_c + \lambda_{\tilde{c}} + \lambda_r + \lambda_{\tilde{r}})v^* = v^* \tag{5.16}$$

Additionally, we recover an homogeneous pattern when $\lambda_c = \lambda_{\tilde{c}} = \lambda_r = \lambda_{\tilde{r}} = \frac{1}{4}$ since

$$\frac{1}{4}(\nu_k^c + \tilde{\nu}_k^c + \nu_j^r + \tilde{\nu}_j^r) = \frac{1}{4}(\nu_k^c + \nu_{N_c^*-(k-1)}^c + \nu_j^r + \nu_{N_r^*-(k-1)}^r)$$
$$= \frac{1}{4}(2v^* + 2v^*) \tag{5.17}$$
$$= v^*, \forall k = 1, ..., N_c^*, j = 1, ..., N_r^*$$

(a) $(\lambda_c, \lambda_{\tilde{c}}, \lambda_r, \lambda_{\tilde{r}}) = (0.5, 0, 0.5, 0)$ (b) $(\lambda_c, \lambda_{\tilde{c}}, \lambda_r, \lambda_{\tilde{r}}) = (0, 0.5, 0, 0.5)$
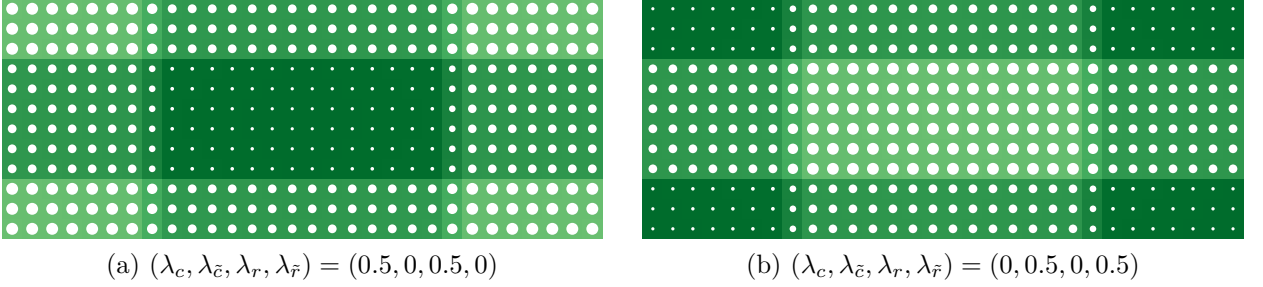
Figure 5.7: Examples of plates built with the convex combinations defined in 5.14 using initial patterns created with parameters $v^* = 0.15$ and $\mu = 0.01$. (a) $(\lambda_c, \lambda_{\tilde{c}}, \lambda_r, \lambda_{\tilde{r}}) = (0.5, 0, 0.5, 0)$. (b) $(\lambda_c, \lambda_{\tilde{c}}, \lambda_r, \lambda_{\tilde{r}}) = (0, 0.5, 0, 0.5)$. The darker the cell the greater the effective density.

We use patterns with $v^* = 0.15$ and $\mu = 0.002$ to illustrate the results, taking into account that for other mean volume fractions the changes are qualitatively the same, but the ranges of reachable elastic parameters changes, as seen in Figure 5.5. Additionally, results presented in Section 5.2 can be derived as a particular case of the combinations presented here, taking $\lambda_r = \lambda_{\tilde{r}} = 0$ to combine only R-symmetric patterns and $\lambda_c = \lambda_{\tilde{c}} = 0$ to combine L-symmetric patterns.

Figure 5.8 shows combinations of pairs of the four main patterns in the $E_L - E_R$ plane. To do that, we define a parameter $\lambda \in [0, 1]$ which combines the two desired patterns, while ignoring the others. As λ changes, a straight line is created between the initial patters, morphing its elastic parameters into one another. With this method it is possible to reach every pair of values of E_L and E_R in between the initial ones.

The four initial patterns and its combinations depicted in Figure 5.8 create a convex hall. All the pairs of elastic parameters inside of it can be reached with convex combinations between the initial patterns, while keeping the same mean volume fraction and effective density. Besides, the convex hall shrinks around the point of the homogeneous pattern when taking greater values of μ, because the range of reachable values decrease when taking less pronounced volume gradients (as explained in Section 5.2).
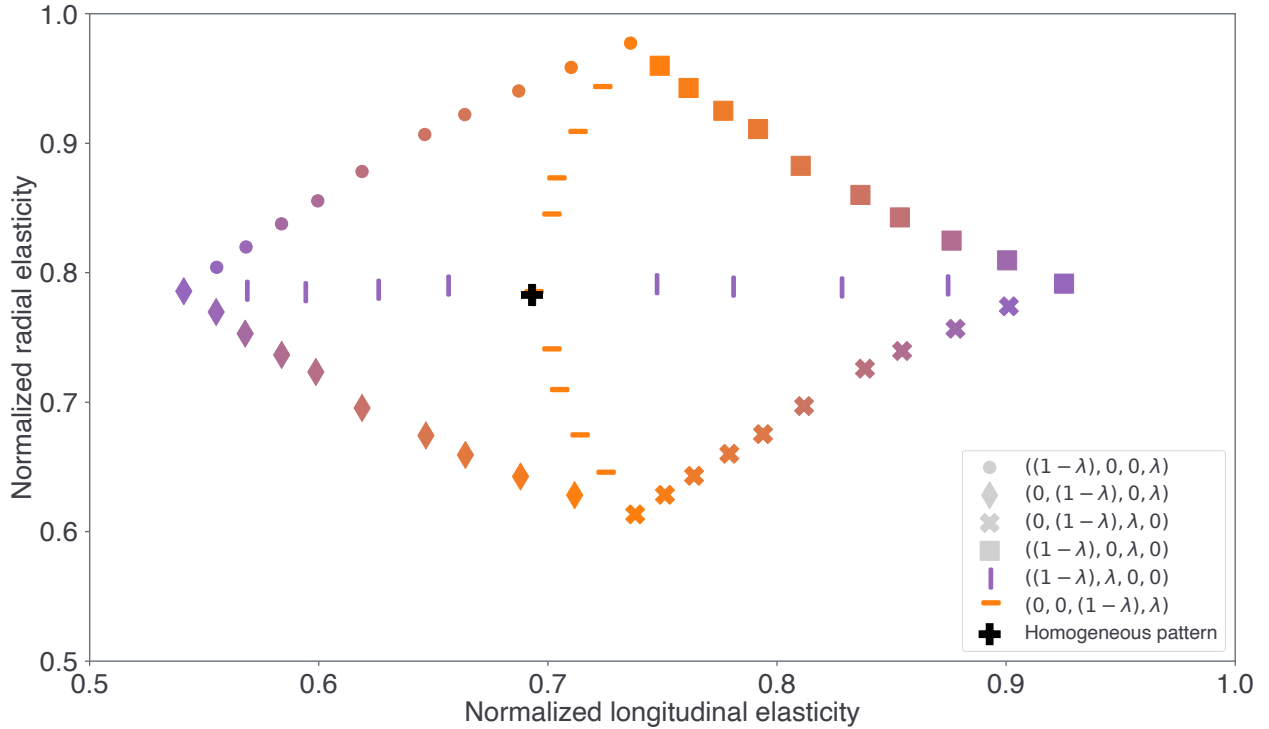
Figure 5.8: $E_L - E_R$ plot (normalized by Engelmann Spruce elastic parameters) for initial patterns with $v^* = 0.15$, $\mu = 0.002$ and its convex combinations. The color of the dot represents the predominant symmetry, where R-symmetric patterns are depicted in purple and L-symmetric ones in orange. With this method it is possible to reach every pair of values of E_L and E_R in between the initial ones, and every pair inside the convex hall preserving the effective density.

To conclude, Figure 5.9 shows the convex hall for several mean volume fractions with $\mu = 0,002$. As stated before, the effect of the combinations is qualitatively the same, but the convex hall changes its size depending on v^*, since the reachable values also changes. These opens the possibility to reach (E_L, E_R) pairs not only with different geometries with the same effective density, but also with geometries that do not share ρ', opening several paths to follow when designing the plate instrument's soundboards.
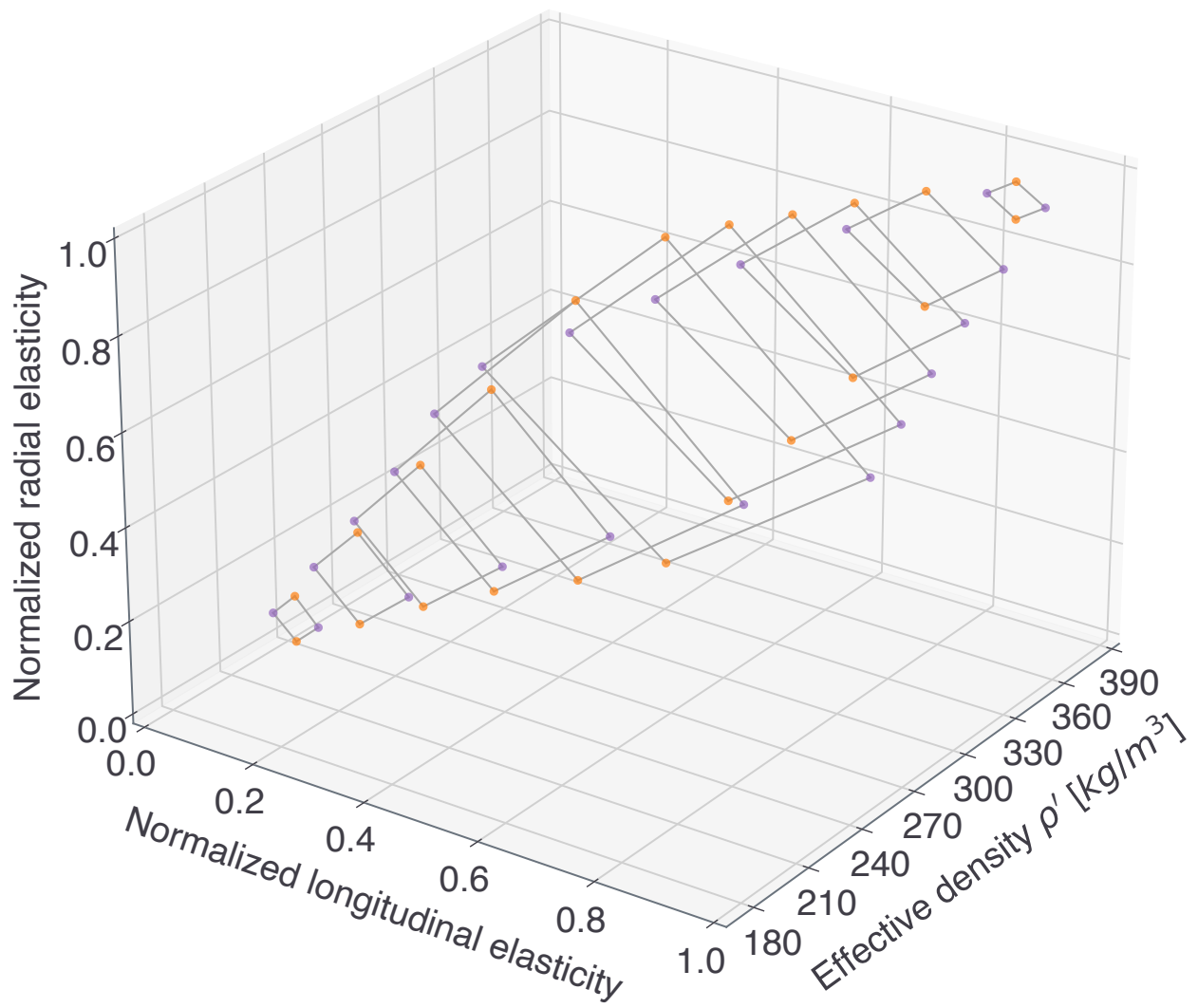
Figure 5.9: 3D plot representing the $E_L - E_R$ (normalized by Engelmann Spruce elastic parameters) plane for several effective densities. Purple and orange dots represent values for R-symmetric and L-symmetric patterns respectively, while gray lines depict the convex hall created combining patterns with the same effective density. Geometries were built taking $\mu = 0.002$.

Chapter 6

Algorithmic optimization

In this chapter an optimization algorithm is described to find the best volume fraction distribution to match target density and elastic parameters. We give a detailed description of the algorithm and two examples of use related to guitar-making.

6.1.   Description

Results presented in Section 5.3 open the possibility to use convex combinations between heterogeneous patterns to match desired density and elastic properties. That is to say, given target parameters (ρ^t, E_L^t, E_R^t), it is possible to found the best convex combination which minimizes the difference between the desired and effective material parameters. With that motivation in mind, we developed an optimization algorithm loosely based on gradient techniques.

The algorithm receives the following information:

- The 10 parameters that describe the source wood:

$$(\rho^s, E_L^s, E_R^s, E_T^s, G_{LR}^s, G_{RT}^s, G_{LT}^s, \nu_{LR}^s, \nu_{RT}^s, \nu_{LT}^s)$$

  These values are used to define a COMSOL model of the wood plate where the patterns per iteration are evaluated.

- 3 target parameters (ρ^t, E_L^t, E_R^t), also called objective parameters.

- A steepness parameter μ, a step size $\alpha > 0$, a threshold $\tau > 0$, and a maximum number of iterations N_{iter}.

and its output correspond to the matrix $\mathcal{V}^*$ with the volume fraction per hole of the optimum pattern. In each iteration of the algorithm, the COMSOL model is evaluated through the *mph* Python package. Python carries the iterative process, receives and output all the parameters.

6.2. Implementation

To measure the distance between the target parameters and the effective parameters of the plate we define the loss function: for $k = 1, ..., N_{iter}$

$$\mathcal{L}^k = |\varepsilon_\rho^k| + |\varepsilon_L^k| + |\varepsilon_R^k| \qquad (6.1)$$

whit

$$\varepsilon_\rho^k = \frac{\rho^t - \rho^k}{\rho^t}, \varepsilon_L^k = \frac{E_L^t - E_L^k}{E_L^t}, \varepsilon_R^k = \frac{E_R^t - E_R^k}{E_R^t} \qquad (6.2)$$

with (ρ^k, E_L^k, E_R^k) the effective parameters in the k-th iteration. $\varepsilon_\rho^k, \varepsilon_L^k$, and ε_R^k measures the error between the target parameters and the effective parameters per iteration.

The iterative process of the algorithm is the following:

1. Initialize the four main heterogenous patterns $\mathcal{V}_c, \mathcal{V}_{\tilde{c}}, \mathcal{V}_r, \mathcal{V}_{\tilde{r}}$ with objective volume fraction $v^t = 1 - \frac{\rho^t}{\rho^s}$ and steepness parameter μ, as method described in Section 5.1. Additionally, we initialize the convex combination parameters as

$$(\lambda_c^1, \lambda_{\tilde{c}}^1, \lambda_r^1, \lambda_{\tilde{r}}^1) = (0.25, 0.25, 0.25, 0.25) \qquad (6.3)$$

These values start the algorithm with an homogeneous pattern of circles. Hence,

$$\mathcal{V}_{ij}^1 = v^*, \mathcal{P}_{ij}^1 = (v^*, 1, 0), \forall i = 1, \ldots, N_r, j = 1, \ldots, N_c \qquad (6.4)$$

Finally,

$$(\rho^1, E_L^1, E_R^1) = (\rho^s, E_L^s, E_R^s) \qquad (6.5)$$

2. For $k = 2, ..., N_{iter}$: the first step is to check if α is bigger enough to make negative any of the convex combination constants, in order to change the learning rate in that case:

   - if $\min(\lambda_c^{k-1}, \lambda_{\tilde{c}}^{k-1}, \lambda_r^{k-1}, \lambda_{\tilde{r}}^{k-1}) < \alpha$:

   $$\alpha = \min(\lambda_c^{k-1}, \lambda_{\tilde{c}}^{k-1}, \lambda_r^{k-1}, \lambda_{\tilde{r}}^{k-1}) \qquad (6.6)$$

   - else:
     do nothing

   Next, the convex combination parameters are updated:

   - If $|\varepsilon_L^{k-1}| \leq |\varepsilon_R^{k-1}|$:

   $$\begin{aligned}
   \lambda_c^k &= \lambda_c^{k-1} + \alpha \mathbb{1}_{\{sign(\varepsilon_L^{k-1})=1\}} - \frac{\alpha}{3} \mathbb{1}_{\{sign(\varepsilon_L^{k-1})=-1\}} \\
   \lambda_{\tilde{c}}^k &= \lambda_{\tilde{c}}^{k-1} - \frac{\alpha}{3} \mathbb{1}_{\{sign(\varepsilon_L^{k-1})=1\}} + \alpha \mathbb{1}_{\{sign(\varepsilon_L^{k-1})=-1\}} \\
   \lambda_r^k &= \lambda_r^{k-1} - \frac{\alpha}{3} \\
   \lambda_{\tilde{r}}^k &= \lambda_{\tilde{r}}^{k-1} - \frac{\alpha}{3}
   \end{aligned} \qquad (6.7)$$

- else:

$$\lambda_c^k = \lambda_c^{k-1} - \frac{\alpha}{3}$$

$$\lambda_{\tilde{c}}^k = \lambda_{\tilde{c}}^{k-1} - \frac{\alpha}{3}$$

$$\lambda_r^k = \lambda_r^{k-1} + \alpha \mathbb{1}_{\{sign(\varepsilon_R^{k-1})=1\}} - \frac{\alpha}{3} \mathbb{1}_{\{sign(\varepsilon_R^{k-1})=-1\}} \qquad (6.8)$$

$$\lambda_{\tilde{r}}^k = \lambda_{\tilde{r}}^{k-1} - \frac{\alpha}{3} \mathbb{1}_{\{sign(\varepsilon_R^{k-1})=1\}} + \alpha \mathbb{1}_{\{sign(\varepsilon_R^{k-1})=-1\}}$$

After updating those parameters, we define the new void matrix as:

$$\mathcal{V}^k := \lambda_c^k \mathcal{V}_c + \lambda_{\tilde{c}}^k \mathcal{V}_{\tilde{c}} + \lambda_r^k \mathcal{V}_r + \lambda_{\tilde{r}}^k \mathcal{V}_{\tilde{r}}, \qquad (6.9)$$

which leads to update the COMSOL model with the new volume fractions. Then, the eigefrequencies and elastic paramers are calculated to obtain the values (ρ^k, E_L^k, E_R^k) of the k-th iteration.

The algorithm has 3 stop criteria:

- If $\mathcal{L}^k < \tau$ or $\min(\lambda_c^k, \lambda_{\tilde{c}}^k, \lambda_r^k, \lambda_{\tilde{r}}^k) = 0$ or $k = N_{iter}$:
  break the cycle

- else:
  go to iteration $k + 1$

3. Return $\mathcal{V}^*$, the optimum of the algorithm.

The way in which $(\lambda_c^k, \lambda_{\tilde{c}}^k, \lambda_r^k, \lambda_{\tilde{r}}^k)$ is updated in every iteration ensures that none of the values become negative and

$$\lambda_c^k + \lambda_{\tilde{c}}^k + \lambda_r^k + \lambda_{\tilde{r}}^k = 1, \forall k = 1, ..., N_{iter} \qquad (6.10)$$

keeping the effective density constant in every iteration. Hence, $\varepsilon_\rho^k = 0, \forall k = 1, ..., N_{iter}$.

The hardware used for running the algorithm was a late 2013 MacBook Pro with an Intel® Core i7 CPU at 2.3 GHz and 16 GB of RAM. Using this computer each iteration takes 40 seconds on average, from which the majority of the time is used in calculating the eigenvalues and eigenfrequencies of the plate.

6.3. Results

In this section we present two use cases for the optimization algorithm. First, we optimize the parameters between two wooden plates made of Engelmann Spruce but with different ρ, E_L, and E_R. This application is inspired by material variability, so the objective is to reduce the variation for wooden plates of the same species. Then, we optimize the difference in ρ, E_L, and E_R of two wooden plates from different species, taking a Western Hemlock plate as source wood while Engelmann Spruce parameters as target. With this example we show that it is possible to "improve" Western Hemlock mechanical behavior for its use in instrument-making. For the rest of this section, we use $\alpha = 0.03, \tau = 0.01$, and $\mu = 0.002$.

6.3.1. Matching between the same wood species

The first experiment consists in matching parameters between woods of the same species. We optimize the mechanical parameters between two wooden plates of Engelmann spruce, but the target one has $\rho^t = 327.25[kg/m^3]$, $E_L^t = 5.91[GPa]$, and $E_R^t = 0.79[GPa]$, while the source plate has the parameters in Table 3.1. The target values are known to be inside the domain described by the four main patterns for the given effective density, so we are also testing the convergence of the algorithm for a value which we know is achievable.

Results from the optimization are summarized in Figure 6.1. As seen in Figure 6.1 (a), after 18 iterations the loss functions takes a value smaller than $\tau = 0.01$ and the algorithm stops, succesfully aproximating the target parameters. Figure 6.1 (b) shows the $E_L - E_R$ plane normalized by the original values of Engelmann Spruce. Clearly, the trajectory of the elastic parameters per iteration (purple) ends close to the target values (red star), resulting in the geometry depicted in Figure 6.1 (c). As a result, the algorithm shows its effectiveness in reducing material variability, founding optimal geometries in a reasonable time.
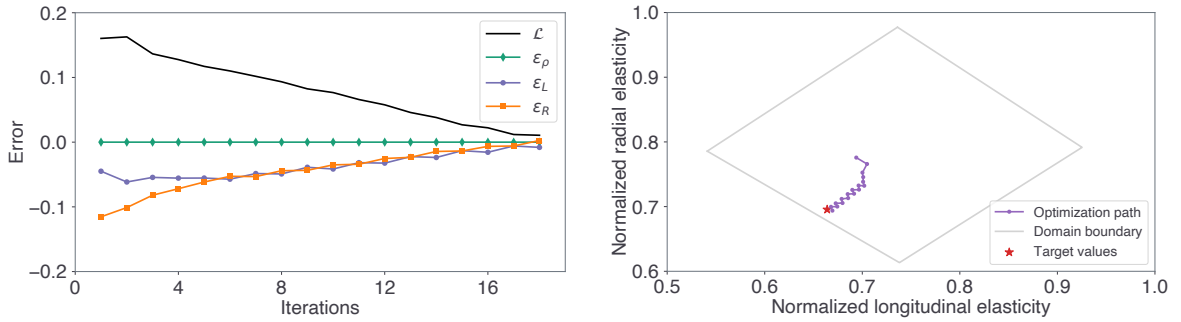
(a) Errors and loss function per iteration.

(b) Trajectory of the elastic parameters per iteration in the $E_L - E_R$ plane, normalized by the source wood parameters.
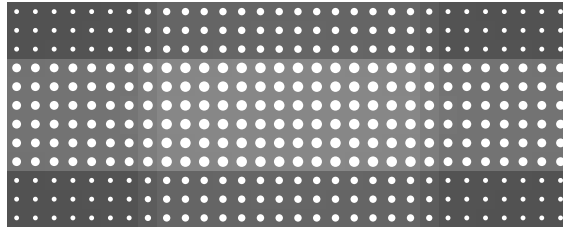
(c) Final plate. The darker the cell the greater the effective density.

Figure 6.1: Summary of the results of optimizing two wooden plates made of Engelmann Spruce but with different ρ, E_L, and E_R. As the target elastic parameters value stays within the domain for ρ^t, the algorithm successfully converge with the given tolerance.

6.3.2. Wood matching between different species

The following example resembles the application in which a matching is performed between plates from two different wood species. In this case, we star with a plate of Western Hemlock as source (its elastic parameters are presented in 7.1), and we want to match the parameters of

a plate made of Engelmann spruce, so $\rho^t = 385[kg/m^3]$, $E_L^t = 8.9[GPa]$, and $E_R^t = 1.13[GPa]$. Since $E_R^t/E_R^s \approx 1.73$, the target value falls outside any possible domain (since it is not possible to reach such higher values), so this examples also works to study how the algorithm behaves when the target elastic parameters are not reachable.

Result from the optimization are summarized in Figure 6.2. After 22 iterations the algorithms stops because $\lambda_c = \lambda_{\tilde{c}} = 0$. Still, as seen in Figure 6.2 (a) the error constantly decrease until the final iteration, showing that even though the minimum is far from optimal, it lends to better results than the initial plate without holes. Figure 6.2 (b) shows the $E_L - E_R$ plane normalized by the source parameters, with the trajectory of the optimization and the target value. It is clear why the value of the loss function is still relatively large, since the target value is outside the domain for the target effective density. The algorithms ends in the upper part of the domain, creating the pattern shown in Figure 6.2 (c).
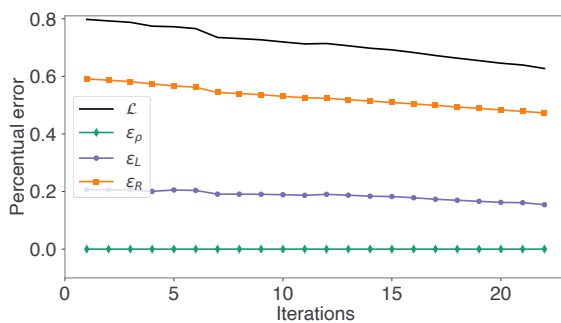
(a) Errors and loss function per iteration.
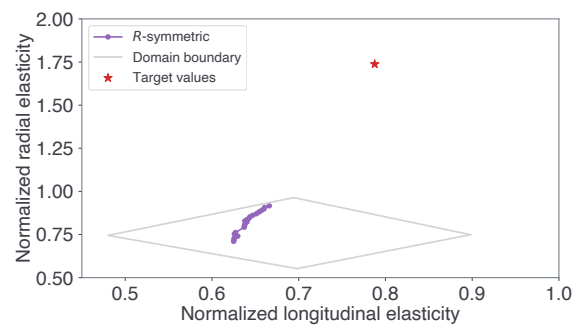
(b) Trajectory of the elastic parameters per iteration in the $E_L - E_R$ plane, normalized by the source wood parameters.
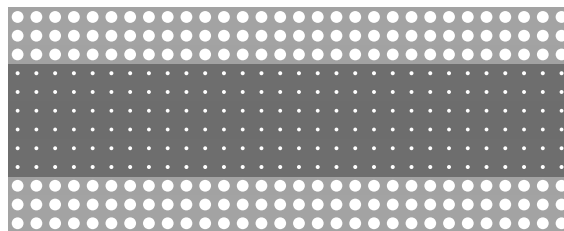
(c) Final plate. The darker the cell the greater the effective density.

Figure 6.2: Summary of the results of optimizing two wooden plates made of different wood species. Even though the algorithm reduce the error between the source and target woods, the final plate elastic parameters are still far from the target ones, since the latter are outside the domain for ρ^t.

Even though the results are not as good as in the previous example, the algorithm successfully get the two wood species closer. The results also evidence how the source wood influence the optimization, as in this case the difference in E_R between woods was crucial. The "ideal" source wood should have greater values for every one of the parameters to be optimized, as we know from the results of previous chapters that it is not possible to surpass the elastic parameters of the plate without holes.

Chapter 7

Conclusion

Guitars have been constantly evolving. Looking for strong yet light soundboards, luthiers have innovated both in materials used and in the structure itself. On top of that, the emerging tonewood scarcity caused by climate change has forced guitar-makers to rely on cheaper woods that are not as well-suited as the traditional ones. This context has motivated luthiers and scientist to research in alternative materials for guitars and wooden instruments in general. In this thesis, we propose wooden mechanical metamaterials as a novel material for instrument-making, whose geometry consists in two main types of hole patterns: i) homogeneous geometries in which every hole has the same size and shape, and ii) heterogeneous patterns of circular holes with different size. We studied how elastic properties change with patterns variations, aiming for a material that let us design the acoustic behavior of wood.

With respect to homogeneous patterns, the effect on the mechanical parameters depends on the hole size and shape. First, we showed that increasing the hole size decreases the value of E_L and E_R. Then, by introducing asymmetries on the hole shape, we can reach several values of these elastic parameters for a fixed effective density. We found that by using asymmetric holes it is possible to change E_L and E_R almost independently, providing the ability to fine tune one of them barely modifying the other. As a result, even though all homogeneous patterns decrease E_L and E_R compared to the values without holes, we found geometries that induced lower anisotropy ratio and higher acoustic radiation, improving the plate response in terms of these quantities.

Later, we found that heterogeneous patterns with different density distributions makes possible to keep the effective properties close to the ones of the plate without holes, with up to 30 % less density. These patterns preserve the independence showed by homogeneous patterns, but reaching values that the latter could not. Depending on the symmetries of the density distribution it its possible to increase or decrease E_L and E_R both independently or at the same time.

Finally, based on the findings, we developed an optimization algorithm to find the best patterned metamaterial to match a given set of target mechanical parameters. We were able to show the effectiveness of our algorithm in two cases which resembles both difficulties that inspired the investigation and affect the guitar-making world, proving that wooden mechanical metamaterials could provide solutions for luthier's needs.

The contribution of this thesis has been to prove that wood elastic parameters can be tuned using mechanical metamaterials. We have shown that now it is possible to choose wood elastic properties and design the best geometry for them. Applications of these novel materials could be many, but in the case of guitar-making the appear as a possible approach to mitigate wood variability and scarcity. With this approach we can reduce the variations between wooden plates from the same species, mitigating one of the largest source of variability in the industry. Additionally, we can match the elastic properties between woods from different species, improving the response of wood naturally not well-suited for instruments. By enhancing the wood types used for instrument making, we can address the present and future scarcity of traditional woods with materials that do not lose the nature of wood tonal characteristics.

This investigation opens many paths to follow. Regarding directly to the results presented, studies of heterogeneous patterns with asymmetric (elliptic) holes could be done in order to find (or not) new reachable values. Those results could be used to improve the optimization algorithm in order to give luthiers more possibilities to build plates. Additionally, from a theoretical point of view, homogenization approaches could help to understand how geometrical characteristics change the effective elasticity tensor and the complete elastic behavior (not only E_L and E_R) at the scale of the effective material [63], explaining the changes in the eigenmodes shape for angle variations in the homogeneous patterns.

Additionally, simulations of whole instruments and experimental validation could be made. It is important to understand the effect of this new material when it is part of a more complex acoustical system, so state of the art simulations could easily accommodate these metamaterials both for classical and archtop guitars [64, 65, 66], or even newly shaped violins [67, 28]. Besides, experimental validation of the observed behavior must be made, both for plates by themselves and for finished instruments. With these results we can proactively tackle the future tonewood scarcity while at the same time open the design space for all instruments with a wooden soundboard, without necessarily resorting to synthetic materials [67] and keeping the historical aesthetic of wooden instruments.

Bibliography

[1] C. Carlier, A. Alkadri, J. Gril, and I. Brémaud, "Revisiting the notion of "resonance wood" choice: a decompartementalised approach from violin makers' opinion and perception to characterization of material properties' variability," in *Wooden musical instruments - Different forms of knowledge : Book of end of WoodMusICK COST Action FP1302*, Cité de la Musique - Philharmonie de Paris, 2018.

[2] S. Merchel, M. E. Altınsoy, and D. Olson, "The natural variability of spruce soundboards: Perceptual differences in the in the tonal quality of acoustic guitars," *The Journal of the Acoustical Society of America*, vol. 146, pp. 2908–2909, 10 2019.

[3] J. Lenoir, J. Gégout, P. Marquet, P. De Ruffrayand, and H. Brisse, "A significant upward shift in plant species optimum elevation during the 20th century," *science*, vol. 320, pp. 1768–1771, 2008.

[4] C. J. Maxwell and R. M. Scheller, "Identifying habitat holdouts for high elevation tree species under climate change," *Frontiers in Forests and Global Change*, vol. 2, p. 94, 2020.

[5] P. Runwal, "Climate change hits rock and roll as prized guitar wood shortage looms." https://www.scientificamerican.com/article/climate-change-hits-rock-and-roll-as-prized-guitar-wood-shortage-looms1/, October 2020.

[6] L. Music. https://www.lavamusic.com.

[7] Rainsong. https://www.rainsong.com.

[8] Ovation. https://www.ovationguitars.com.

[9] Blackbird. https://www.blackbirdguitar.com.

[10] X. Yu, J. Zhou, H. Liang, Z. Jiang, and L. Wu, "Mechanical metamaterials associated with stiffness, rigidity and compressibility: A brief review," *Progress in Materials Science*, vol. 94, p. 114–173, 2018.

[11] C. E. Oñate, A. Arancibia, G. Cartes, and C. F. Beas, "Seeking for spectral manipulation of the sound of musical instruments using metamaterials," in *Proceedings of the 15th International Conference on Audio Mostly*, pp. 277–280, 2020.

[12] R. Bader, J. Fischer, M. Münster, and P. Kontopidis, "Metamaterials in musical acoustics: A modified frame drum," *The Journal of the Acoustical Society of America*, vol. 145, no. 5, pp. 3086–3094, 2019.

[13] G. Caldersmith and E. Freeman, "Wood properties from sample plate measurements i," *J Catgut Acoust Soc*, vol. 1, no. series II, pp. 8–12, 1990.

[14] J. Montagu, *Origins and development of musical instruments.* Lanham, Md: Scarecrow Press, 1 ed., 2007.

[15] R. Courtnall, *Making master guitars.* London, Hale, 2007.

[16] J. Tyler and P. Sparks, *The Guitar and Its Music: From the Renaissance to the Classical Era.* Early music series, Oxford University Press, 2002.

[17] C. Cooper, "Gernot wagner: The master luthier on the double-top movement and his influences." https://classicalguitarmagazine.com/gernot-wagner-the-master-luthier-on-the-double-top-movement-and-his-influences-2/, August 2006.

[18] M. Dominelli, "Double top construction." https://www.dominelliguitars.com/tech-talk/double-top-construction.html.

[19] its-all-about guitar.com, "Acoustic guitar anatomy." http://www.its-all-about-guitar.com/acoustic-guitar-anatomy.html.

[20] J. Rogers, "Modern classical guitar design part 6: Double top." https://nbnguitar.com/nbn-guitar-blog/modernclassicalguitardesignpart6-doubletop.

[21] U. G. K. Wegst, "Wood for sound," *American Journal of Botany*, vol. 93, pp. 1439–1448, 10 2006.

[22] S. Yoshikawa, "Acoustical classification of woods for string instruments," *Journal of the Acoustical Society of America*, vol. 122, p. 568, 2007.

[23] T. Noguchi, E. Obataya, and K. Ando, "Effects of aging on the vibrational properties of wood," *Journal of Cultural Heritage*, vol. 13, no. 3, Supplement, pp. S21–S25, 2012. Wood Science for Conservation.

[24] P. Dumond and N. Baddour, "Can a brace be used to control the frequencies of a plate?," *SpringerPlus 2*, vol. 558, 10 2013.

[25] A. Pfriem, "Thermally modified wood for use in musical instruments," *Drvna Industrija*, vol. 66, pp. 251–253, 09 2015.

[26] H. Yano, H. Kajita, and K. Minato, "Chemical treatment of wood for musical instruments," *The Journal of the Acoustical Society of America*, vol. 96, no. 6, pp. 3380–3391, 1994.

[27] C. Dunn, "Analyzing the acoustical properties of alternative materials in guitar soundboards to reduce deforestation," *ResearchGate*, 06 2013.

[28] S. Gonzalez, D. Salvi, D. Baeza, F. Antonacci, and A. Sarti, "A data-driven approach to violin making," *Scientific Reports*, vol. 11, no. 1, pp. 1–9, 2021.

[29] V. Veselago, "The electrodynamics of substances with simultaneously negative values of ε and μ," *Physics-Uspekhi*, vol. 10.4, pp. 509–514, 1968.

[30] J. Pendry, "Negative refraction makes a perfect lens," *Physical Review Letters*, vol. 85.18, p. 3966, 2000.

[31] W. Cai and V. Shalaev, *Optical Metamaterials: fundamentals and applications.* Springer New York Dordrecht Heidelberg London, 2010.

[32] M. Wegener, "Metamaterials beyond optics," *Science*, vol. 342.6161, pp. 939–940, 2013.

[33] G. Pacchioni, "Mechanical metamaterials: the strength awakens," *Nature reviews materials*, 2016.

[34] X.-F. Li *et al.*, "Tunable unidirectional sound propagation through a sonic-crystal-based acoustic diode," *Physical Review Letters*, vol. 106.8, p. 084301, 2011.

[35] T. Bückmann *et al.*, "An elasto-mechanical unfeelability cloak made of pentamode metamaterials," *nature communications*, vol. 4130, 2014.

[36] Z. Yang *et al.*, "Acoustic metamaterial panels for sound attenuation in the 50-1000 hz regime," *Applied physics letters*, vol. 96.4, p. 041906, 2010.

[37] K. Bertoldi, P. Reis, S. Willshaw, and T. Mullin, "Negative poisson's ratio behavior induced by an elastic instability," *Advanced Materials*, vol. 22, pp. 361–366, 2010.

[38] J. Overvelde, S. Shan, and K. Bertoldi, "Compaction through buckling in 2d periodic, soft and porous structures: Effect of pore shape," *Advanced Materials*, vol. 24, pp. 2337–2342, 2012.

[39] Q. Wang, J. Jackson, Q. Ge, J. Hopkins, C. Spadaccini, and N. Fang, "Lightweight mechanical metamaterials with tunable negative thermal expansion," *Physical Review Letters*, vol. 117, 2016.

[40] B.-B. Zheng, M.-H. Fu, W.-H. Li, and L.-L. Hu, "A novel re-entrant honeycomb of negative thermal expansion," *Smart Materials and Structures*, vol. 27, 2018.

[41] T. Tachi, "Designing Freeform Origami Tessellations by Generalizing Resch's Patterns," *Journal of Mechanical Design*, vol. 135, 10 2013.

[42] J. Surjadi, L. Gao, D. Huifeng, X. Li, X. Xiong, N. Fang, and Y. Lu, "Mechanical metamaterials and their engineering applications," *Advanced Engineering Materials*, vol. 21, 2019.

[43] X. Zheng, H. Lee, T. H. Weisgraber, M. Shusteff, J. DeOtte, E. B. Duoss, J. D. Kuntz, M. M. Biener, Q. Ge, J. A. Jackson, S. O. Kucheyev, N. X. Fang, and C. M. Spadaccini, "Ultralight, ultrastiff mechanical metamaterials," *Science*, vol. 344, no. 6190, pp. 1373–1377, 2014.

[44] A. Alderson, K. Alderson, D. Attard, K. Evans, R. Gatt, J. Grima, W. Miller, N. Ravirala, C. Smith, and K. Zied, "Elastic constants of 3-, 4- and 6-connected chiral and anti-chiral honeycombs subject to uniaxial in-plane loading," *Composites Science and Technology*, vol. 70, no. 7, pp. 1042–1048, 2010. Special issue on Chiral Smart Honeycombs.

[45] E. Özdemir, L. Kiesewetter, K. Antorveza, T. Cheng, S. Leder, D. Wood, and A. Menges, "Towards self-shaping metamaterial shells," in *Proceedings of the 2021 DigitalFUTURES*, pp. 275–285, Springer Singapore, 2022.

[46] G. Iannace, G. Ciaburro, and A. Trematerra, "Metamaterials acoustic barrier," *Applied Acoustics*, vol. 181, p. 108172, 2021.

[47] C. Lagarrigue, J. Groby, and V. Tournat, "Sustainable sonic crystal made of resonating bamboo rods," *The Journal of the Acoustical Society of America*, vol. 133, 2013.

[48] Y. Liu, J. Huang, Y. Li, and Z. Shi, "Trees as large-scale natural metamaterials for low-frequency vibration reduction," *Construction and Building Materials*, vol. 199, pp. 737–

745, 2019.

[49] M. Kitahara, *Boundary integral equation methods in eigenvalue problems of Elastodynamics and Thin Plates.* Elsevier, 1985.

[50] L. Landau and E. Lifshitz, *Theory of Elasticity, 2nd ed.* Pergamon Press, 1970.

[51] G. Allaire, *Shape optimization by the homogenization method, volume 146.* Springer, 2002.

[52] P. Lax, *Functional Analysis.* John Wiley & Sons, Inc., 2002.

[53] A. A. Mokhtari, Y. Lu, and A. Srivastava, "On the properties of phononic eigenvalue problems," *Journal of the Mechanics and Physics of Solids*, vol. 131, pp. 167–179, 2019.

[54] A. Boresi, R. Schmidt, and O. Sidebottom, *Advanced mechanics of materials.* John Wiley & Sons, Inc., 1992.

[55] R. J. Ross *et al.*, *Wood handbook: wood as an engineering material*, vol. 190. University of Wisconsin, 2010.

[56] E. Obataya, M. Norimoto, and J. Gril, "The effects of adsorbed water on dynamic mechanical properties of wood," *Polymer*, vol. 39, no. 14, pp. 3059–3064, 1998.

[57] T. Ono, "Frequency responses of wood for musical instruments in relation to the vibrational properties," *Journal of the Acoustical Society of Japan (E)*, vol. 17, no. 4, pp. 183–193, 1996.

[58] J. Schelleng, "The violin as a circuit," *Journal of the Acoustical Society of America*, vol. 35, p. 326, 1963.

[59] E. Obataya, M. Norimoto, and J. Gril, "Effects of natural and artificial ageing on the physical and acoustic properties of wood in musical instruments," *Journal of Cultural Heritage*, vol. 27, pp. S63–S69, 2017. Wooden Musical Instruments Special Issue.

[60] M. McIntyre and J. Woodhouse, "On measuring wood properties, part 2," *Journal Catgut Acoustical Society*, vol. 43, pp. 18–24, 1985.

[61] R. Viala, V. Placet, and S. Cogan, "Simultaneous non-destructive identification of multiple elastic and damping properties of spruce tonewood to improve grading," *Journal of Cultural Heritage*, vol. 42, pp. 108–116, 2020.

[62] J. Hen, M. Elfner, and J. Feder, "Pythonic scripting interface for comsol multiphysics." https://github.com/MPh-py/MPh.

[63] J. Mura and A. Caiazzo, *A Two-Scale Homogenization Approach for the Estimation of Porosity in Elastic Media*, pp. 89–105. Cham: Springer International Publishing, 2016.

[64] A. Brauchler, P. Ziegler, and P. Eberhard, "An entirely reverse-engineered finite element model of a classical guitar in comparison with experimental data," *The Journal of the Acoustical Society of America*, vol. 149, no. 6, pp. 4450–4462, 2021.

[65] T. J. Nania, "Archtop guitar dynamics," *Violin Society of America Papers*, vol. 29, no. 1, pp. 1–13, 2021.

[66] D. Salvi, S. Gonzalez, F. Antonacci, and A. Sarti, "Modal analysis of free archtop guitar top plates," *The Journal of the Acoustical Society of America*, vol. 150, no. 2, pp. 1505–1513, 2021.

[67] T. Duerinck, G. Verberkmoes, C. Fritz, M. Leman, L. Nijs, M. Kersemans, and W. Van Paepegem, "Listener evaluations of violins made from composites," *The Journal of the Acoustical Society of America*, vol. 147, no. 4, pp. 2647–2655, 2020.

Annexes

Annexed A: Mode shapes for homogeneous patterns with different angles

Figure 7.1 shows examples of three homogeneous plates and its first five eigenmodes. With all the ellipses rotating in the same direction, a "smooth" mode switching between the modes $(1,1)$ and $(0,2)$ can be seen, showing a X-mode for an angle of $\pi/4$ (Figure 7.1 (b)). This behavior can only be seen with smooth angle variations, since for aspect ratio variations and heterogeneous configurations the shape of the eigenmodes remains the same and the switching between modes occurs in a "discontinous" manner. The presence of the X-mode and changes in shape could be caused by variations in the relation between stiffness in the orthogonal directions, which translates as changes in the Poisson's ratio values, but the research in that direction goes beyond the scope of this research.

(a) $(v^*, k^*, \theta^*) = (0.30, 2.2, 0)$.　　(b) $(v^*, k^*, \theta^*) = (0.30, 2.2, \frac{\pi}{4})$.　　(c) $(v^*, k^*, \theta^*) = (0.30, 2.2, \frac{\pi}{2})$.
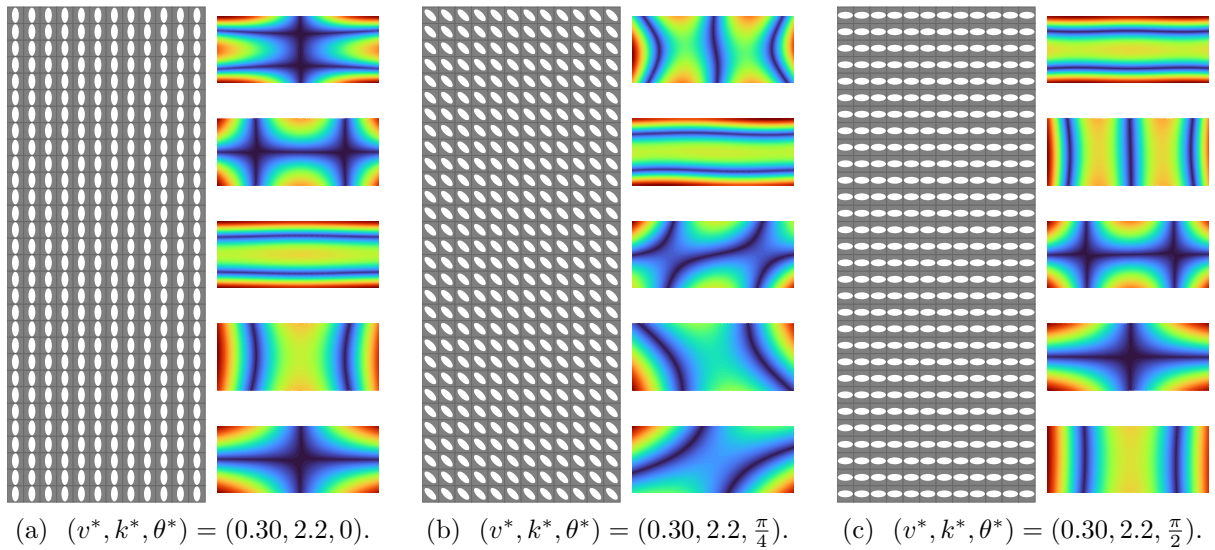
Figure 7.1: Examples of mode shapes for homogeneous plates with different values of θ. In each figure, the plate is oriented with the Longitudinal axis vertical, while the mode are arrenged from bottom to top. The angle of the ellipse with respect to the L-axis influence the 5 first modes shape and order.

Annexed B: Experimental validation of homogeneous results

To validate our predictions, the contributor Carolina Espinoza performed experiments with a book-matched set of Spruce Engelmann typically used for the manufacture of guitar tops. The dimensions of both plates were $a = 550$ mm, $b = 200$ mm and $h = 3.5$ mm. For each sample, we measured the frequencies $f_{2,0}$ and $f_{0,2}$ to obtain their stiffness by applying (3.8). Then, we characterized the elastic changes after cutting three different patterns of ellipses, increasing their size while keeping constant their aspect ratio on each step. One plate, labelled AW, was cut with a pattern of 9×20 ellipses parallel to the R direction. The other, labelled BW, was cut with a pattern of 10×20 ellipses parallel to the L direction. The plates were cut with a ShopBot Desktop 3-axis CNC router. The smallest hole was 2×6 mm, and could be cut accurately with a 1 mm router bit. For the second and third steps on each plate we enlarged the holes to 4×12 mm and to 6×18 mm respectively.

To measure the frequencies of the $(2, 0)$ and $(0, 2)$ modes after each cut, we used the following setup: a swept sine signal was sent by a dynamic signal analyzer (Stanford System SR780) and amplified by a power amplifier (Gemini XGA-5000). The plate, supported by two rubber bands, was vibrated by a loudspeaker placed 1 cm from it. The plate response was measured by a micro-accelerometer (PCB 356A14) connected to a signal conditioner (PCB 408E09) and attached to the plate, 1 cm from one of its corners. Finally, modal identification was performed visually by observing the Chladni patterns. The plates were kept in a humidity-controlled environment between cuts.

Figure 7.2 shows the evolution of the stiffness as a function of the effective density for each plate. As expected from the results of Fig. 4.3 the decay in the stiffness for each plate is dependent on the orientation of the hole with respect to the grain direction. For the radial ellipses the decay in E_L is slower than for the vertical ellipses, and this is reversed when we look at E_R, in agreement with our simulations. Two things must be noted: a) the initial stiffness for the two pieces of wood is not the same even though they come from the same tree and are book-matched; they are also different from the nominal value that we used in our simulations. b) The effective density of the plates is not the same since we needed to remove a row of ellipses in the case of the radially oriented ellipses so the largest hole size could fit in the plate. The results are remarkable since they show that the variation in the mechanical parameters when changing the hole size are robust to varying the number of cells, dimension of the plate, and material parameters of the initial sample, and that is a general property of the wooden metamaterials. However, they also show the need to have a dedicated simulation of the particular material parameters of the initial plate to reproduce or predict the quantitative behavior of the metamaterial.
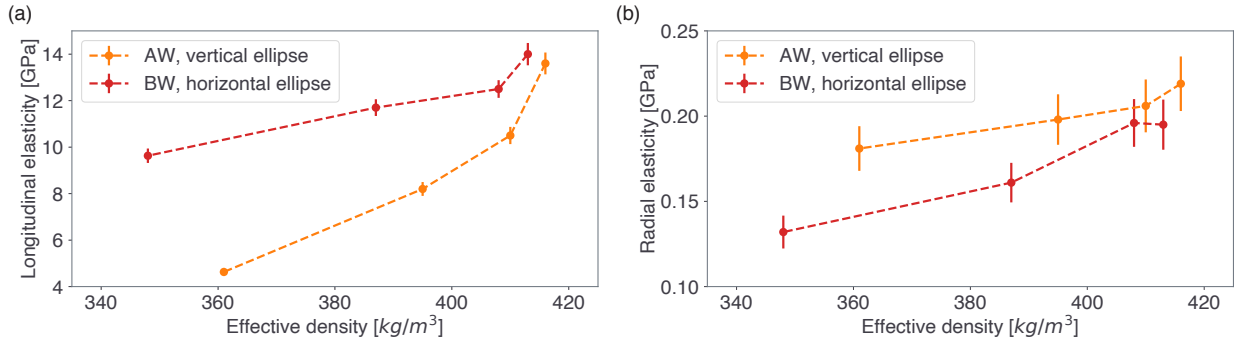
Figure 7.2: Experimental results of the stiffness as a function of the effective density of the plate for two samples. For *AW* the effective density changes between 1 % and 13 % and we observe a decrease between 23 % and 70 % for E_L, and between 6 % and 17 % for E_R. For *BW* the effective density changes between 1 % and 16 % and we observe a decrease between 11 % and 31 % for E_L, and between 0.5 % and 32 % for E_R. The density has an error around 1.1 %. (a) Longitudinal elasticity E'_L vs density ρ'. (b) Radial elasticity E'_R vs density ρ'

Annexed C: Generalization to different woods

To test the generalization of the results to different use cases, we replicated the homogeneous experiments made with Engelmann spruce to different woods with the same plate and cell dimensions, as a way to measure the influence of the initial mechanical parameters in the variations presented in the main chapters. Two types of woods were chosen for this example: Western Hemlock and Western Larch. Values of the elastic properties of both woods can be found in Table 7.1.

Table 7.1: Western Hemlock and Western Larch density and elastic properties. Elastic properties correspond to the ones for both woods reported in [55].

Western Hemlock									
Density [kg/m³]	**Young's Moduli [GPa]**			**Shear Moduli [GPa]**			**Poissons's Ratios**		
ρ	E_L	E_R	E_T	G_{LR}	G_{RT}	G_{LT}	ν_{LR}	ν_{RT}	ν_{LT}
465	11.3	0.65	0.35	0.43	0.03	0.36	0.485	0.442	0.423
Western Larch									
Density [kg/m³]	**Young's Moduli [GPa]**			**Shear Moduli [GPa]**			**Poissons's Ratios**		
ρ	E_L	E_R	E_T	G_{LR}	G_{RT}	G_{LT}	ν_{LR}	ν_{RT}	ν_{LT}
575	12.9	1.02	0.84	0.81	0.09	0.89	0.355	0.389	0.276

Denser woods where chosen with the purpose to test the ability of the optimization algorithm to adjust their elastic parameters to the ones of Engelmann spruce. In addition, woods with higher E_L were chosen because as shown in the main chapters, it is not possible to obtain higher values than the original one when making holes in the plate. Hence, if we want to match woods, it is necessary to start from woods with higher E_L and desirably higher E_R.

We defined the following procedure in order to measure the variation between woods: first, we took the same measures described in 4.3 for every wood with the same dimensions both for plate and cells. Then, for every geometry we calculated the percentage error with respect

to Engelmann Spruce in terms of the normalized density and mechanical parameters. Finally, for every normalized effective density we took the mean error between all the geometries with the same mean volume fraction.

Results from the procedure described above are shown in Figure 7.3. For each wood, both elastic constants share almost the same mean error it shows only slight variations for different effective densities. Western Larch has an overall minor error than Western Hemlock. Despite this difference, both mean errors do not surpass 8 %, showing that the effect of the geometry is the same. Even though the study of the rest of the mechanical parameters exceed the scope of this thesis, the difference in error could be explained with the relationship between the main elastic parameter E_L with the rest of them: the relationships for Western Larch are closer to the ones that Engelmann spruce presents, while Western Hemlock has a much more predominant principal longitudinal direction.
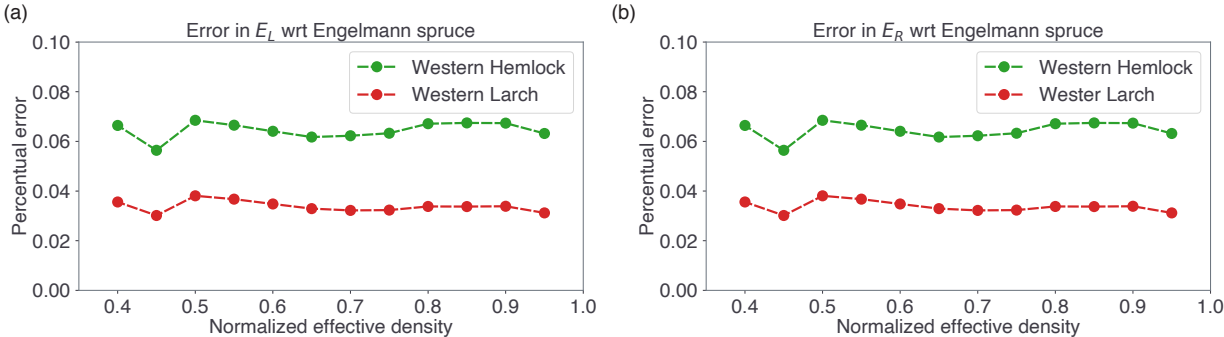

Figure 7.3: Mean percentual error for variations in E'_L and E'_R showed by Western Hemlock and Wester Larch with respect to Engelmann Spruce, for several effective densities. For both cases, Western Larch shows less error than Western Hemlock, while for both of them the error do no surpass 8 %. In addition, in each case the error is almost constant with respect to the effective density. (a) E'_L error. (b) E'_R error.

Annexed D: Generalization to different plate size

We use the same procedure to measure the error, but know using the same wood and a plate with different dimensions. The alternative plate has dimensions $a = 0.28$ and $b = 0.36$, while keeping the same cell size. These dimensions were chosen for two reasons: they allow to measure the effect when the longitudinal axis is smaller than the radial axis, and they represent similar dimensions to the ones on the lower of the guitar soundboard. The latter has an important application when the holes are carved directly in the soundboard without using double-top techniques, as making holes where the bracing of the top plate goes would not have significant effects in the vibrations of the plate.

The obtained errors are shown in Figure 7.4. In this case the error increase when decreasing the effective density, but all of them are still below 8 %.
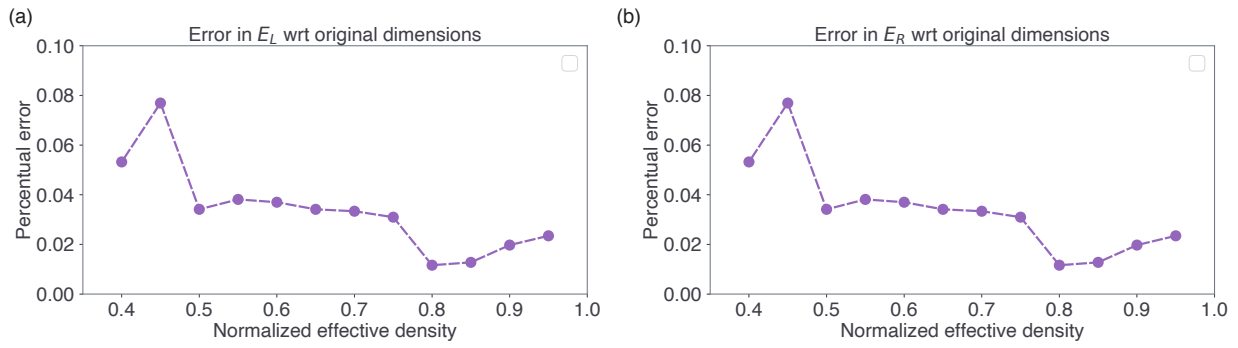
Figure 7.4: Mean percentual error for variations in E'_L and E'_R showed by an alternative plate with respect to the values of the main result, for several effective densities. Both plates are simulated with Engelmann spruce mechanical constants. While the error tends to decrease when the effective density increase, it stays lower than $8\,\%$ for both E'_L and E'_R. (a) E'_L error. (b) E'_R error.